



**UNIVERSITY OF MISKOLC**

Faculty of Earth and Environmental Sciences and Engineering

Department of Geophysics

**Amplitude Versus Offset (AVO) analysis for geothermal  
exploration in the Little Hungarian Plain**

Research topic area:

Intergraded seismic and well logging techniques

**PhD Thesis**

by

**Emad Nageh Masri Abdelnour**

Supervisors:

Dr. Tamás Fancsik

Dr. Ernő Takács

**MIKOVINY SÁMUEL DOCTORAL SCHOOL OF EARTH SCIENCES**

Head of the Doctoral School:

Prof. Dr. Péter Szűcs

Miskolc, Hungary, 2023

**SUPERVISOR'S FOREWORD**

**for the PhD thesis**

**Amplitude Versus Offset (AVO) analysis for geothermal exploration  
in the Little Hungarian Plain written by Emad Nageh Masri Abdelnour**

First time, I met Emad Nageh Masri Abdelnour in July 2018 when he attended a four-week internship at the former Mining and Geological Survey of Hungary. His task was to learn about the integrated well log and seismic data processing and interpretation. After he completed his training, he came into my office with a request that he wants to learn about Amplitude Versus Offset (AVO) analysis. We had a great conversation about the rock physics and seismic wave propagation thus, in January 2019, I undertook the supervision of his master's thesis in AVO analysis applied for hydrocarbon exploration. He joined my course 'Geophysical Interpretation and Prospecting' held for MSc students at the Department of Geophysics, University of Miskolc, Hungary. After graduation, in June 2019, Emad decided to continue his studies as a PhD student. I offered him an exciting but still unrevealed field of research, namely, studying the application possibilities of the AVO analysis for geothermal exploration. At first, he expressed his demand for another topic around the hydrocarbon exploration; but shortly he agreed and started to work very hard to get novel results in a pilot geothermal study area (Little Hungarian Plain, Pannonian Basin).

I guess his decision, four years ago, was right because global energy transition is on the corner, I would rather say it has been started by now. Many companies working in the hydrocarbon industry started to work out their own methodology to explore geothermal reservoirs. It is no wonder because the lithological settings are very similar for both reservoir types. The Candidate, in his PhD dissertation, provided a detailed procedure around the application of seismic inversion for geothermal investigation. He applied not only AVO inversion but also Simultaneous Model-based inversion and Lambda-Mu-Rho transformation to obtain seven different elastic properties of the Triassic basement in his study area.

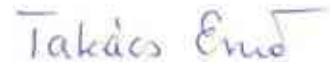
I can say that the Candidate became an experienced researcher in rock physics and seismic inversion during his PhD education. He gained lots of skills about the utilization of several geophysical and geological software (for instance Hampson-Russell, Petrel, Techlog,

and OpendTect). He turned to be out a self-educating person being motivated to learn about programming, as well as Machine and Deep Learning via online courses. I recognized him as an ambitious, apprehensive, and competent PhD candidate. During his work, he always had plans A, B, and C depending on the progress of his research.

I certify that his dissertation contains valid data, and the results are representing the candidate's own work. In my opinion, the thesis is fully adequate in both the scope and quality requirements of the Mikoviny Sámuel Doctoral School of Earth Sciences.

For all the above specified reasons, I recommend Emad Nageh Masri Abdelnour to be awarded with a PhD degree.

24 July 2023, Miskolc

A handwritten signature in blue ink that reads "Takács Ernő".

Dr. Ernő Takács PhD

Supervisor

## CONTENTS

List of figures and tables	iv
Abbreviations	viii
1. INTRODUCTION	1
2. AVO THEORY	3
2.1. Brief historical overview	3
2.2. Rock physical basics	5
2.3. Biot-Gassmann theory	6
2.4. Zoeppritz equations and their approximations	7
2.5. Examples for normal and anomalous AVO responses in clastic sediments	10
3. GEOLOGICAL FRAMEWORK AND GEOPHYSICAL DATASET	12
3.1. Background geology and available geophysical data	12
4. MODELLING AND DATA PREPARATION	14
4.1. AVO modelling based on well log data ( <b>Thesis 1</b> )	14
4.2. True amplitude seismic data pre-processing	19
4.3. Seismic well tie ( <b>Thesis 2</b> )	25
5. INVERTED RESULTS AND DISCUSSION	29
5.1. Traditional post-stack P-impedance inversion ( <b>Thesis 3</b> )	30
5.2. Pre-stack AVO inversion ( <b>Thesis 4</b> )	34
5.3. Pre-stack Simultaneous Model-based inversion ( <b>Thesis 5</b> )	37
5.4. Additional Lambda-Mu-Rho transformation ( <b>Thesis 6</b> )	48
6. TRACKING THE FRACTURE ZONE	54
6.1. Cross-plotting the fracture zone(s)	54
6.2. Spatial mapping of the inverted elastic parameters ( <b>Thesis 7</b> )	58
7. SUMMARY	62
Acknowledgements	65
References	66

List of figures and tables

Figure	Caption	Page
Fig. 1:	$V_P/V_S$ and Poisson's ratio for different rocks and mineral types (Chopra and Castagna 2014)	5
Fig. 2:	Poisson's ratio versus water saturation ( $S_w$ ) for a two-phase water and gas model (Hampson-Russell Software Services Ltd. 2009)	6
Fig. 3:	Rock components: skeleton, pores, and fluid (Hampson-Russell Software Services Ltd. 2009)	6
Fig. 4:	Elastic waves generated at a single interface in case of incident P-wave (modified after Takács et al. 2021)	8
Fig. 5:	Linear regression of the observed pre-stack amplitudes with the square of sin of incident angle (after Chopra and Castagna 2014)	9
Fig. 6:	Normal AVO response (modified after Chopra and Castagna 2014)	11
Fig. 7:	Anomalous AVO response (modified after Chopra and Castagna 2014)	11
Fig. 8:	Location map showing the pre-Cenozoic geology structure of Hungary (modified after Haas et al. 2014)	12
Fig. 9:	Logs from a productive deviated geothermal well (modified after Masri and Takács 2022a)	16
Fig. 10:	Model parameters after blocking the well logs (modified after Masri and Takács 2022a)	17
Fig. 11:	Theoretical AVO responses from the interfaces of the above discussed seven-layer-model (modified after Masri and Takács 2022a)	18
Fig. 12:	CDP gathers close to the location of a productive geothermal well	22
Fig. 13:	CDP gathers after applying trim static corrections	23
Fig. 14:	CDP super gathers after vertical stacking of five adjacent individual CDPs obtained by the earlier application of trim static corrections	24
Fig. 15:	Angle gathers ( $0-44^\circ$ ) calculated from the CDP super gathers	25
Fig. 16:	Results of the seismic well tie (modified after Masri and Takács 2022a)	26
Fig. 17:	Raw P-wave acoustic impedance log before seismic well tie inserted in the seismic section (modified after Masri and Takács 2022a)	27

Fig. 18:	Correlated P-wave acoustic impedance log after seismic well tie inserted in the seismic section (modified after Masri and Takács 2022a)	28
Fig. 19:	Basemap showing the limits of the true amplitude pre-processed 3D seismic data, as well as the locations of the deviated production well and the test profile (modified after Masri and Takács 2022b)	30
Fig. 20:	Original (blue) and inverted (red) P-impedance logs at the location of the well, as well as the synthetic seismic traces (blue) calculated from the inverted data; and the real (black) and error (blue) traces	32
Fig. 21:	Inverted seismic P-wave impedance ( $Z_P$ ) section calculated from post-stack amplitude data, and inserted P-wave impedance log at the location of the well where FR marks the top of the fractured zone and T1 marks its base based on the drilling reports (Masri and Takács 2023)	33
Fig. 22:	Acoustic impedance log after seismic well tie inserted in the Scaled Poisson's Ratio Change AVO attribute cross-section (modified after Masri and Takács 2022a)	35
Fig. 23:	Simplified workflow of the Simultaneous Model-based pre-stack inversion procedure (Masri and Takács 2023)	38
Fig. 24:	P-wave acoustic impedance ( $Z_P$ ) low frequency start model (0-10 Hz) built up based on extrapolated well log data (Masri and Takács 2023)	40
Fig. 25:	Original and inverted P- and S-wave impedance and density logs at the location of the well, as well as the seismic synthetic, real and error traces (Masri and Takács 2023)	42
Fig. 26:	Inverted P-wave impedance ( $Z_P$ ) section calculated from the pre-stack seismic amplitude data and the available well logs (Masri and Takács 2023)	43
Fig. 27:	Inverted S-wave impedance ( $Z_S$ ) section calculated from the pre-stack seismic amplitude data and the available well logs (Masri and Takács 2023)	44
Fig. 28:	Inverted density ( $\rho$ ) section calculated from the pre-stack seismic amplitude data and the available well logs (Masri and Takács 2023)	45
Fig. 29:	Derived $V_P/V_S$ velocity ratio section calculated from the pre-stack	46

	seismic amplitude data and the available well logs (Masri and Takács 2023)	
Fig. 30:	Poisson's ratio versus P-wave velocity parameters for different lithology (redrawn after Miles et al. 1989)	47
Fig. 31:	Scaled Poisson's Ratio Change ( $\Delta\sigma$ ) attribute plot and lithological interpretation with P-wave impedance log inserted at the location of the production well	50
Fig. 32:	$V_P/V_S$ velocity ratio attribute plot and lithological interpretation with P-wave impedance log inserted at the location of the production well	51
Fig. 33:	Lambda*Rho ( $\lambda\rho$ ) attribute plot and lithological interpretation with P-wave impedance log inserted at the location of the production well	52
Fig. 34:	Mu*Rho ( $\mu\rho$ ) attribute plot and lithological interpretation with P-wave impedance log inserted at the location of the production well	53
Fig. 35:	Mu*Rho ( $\mu\rho$ ) versus Lambda*Rho ( $\lambda\rho$ ) parameters for different lithology (after Goodway 2001)	53
Fig. 36:	P- and S-wave velocity ratio ( $V_P/V_S$ ) versus P-impedance ( $Z_P$ ) cross-plots of the inverted seismic data (a and b) and the highlighted zones along the test profile (c)	56
Fig. 37:	Mu*Rho ( $\mu\rho$ ) versus Lambda*Rho ( $\lambda\rho$ ) cross-plots of the inverted seismic data (a and b) and the highlighted zones along the test profile (c)	57
Fig. 38:	Scaled Poisson's Ratio Change ( $\Delta\sigma$ ) map along the a priori estimated top surface of the Triassic geothermal reservoir	58
Fig. 39:	P- and S-wave velocity ratio ( $V_P/V_S$ ) map along the a priori estimated top surface of the Triassic geothermal reservoir	59
Fig. 40:	Lambda*Rho ( $\lambda\rho$ ) map along the a priori interpreted top of the investigated Triassic geothermal reservoir	60

<b>Table</b>	<b>Title</b>	<b>Page</b>
Table 1:	Geology and lithology in a productive geothermal well of the study area (modified after Masri and Takács 2022a)	13
Table 2:	Seven-layer-model based on the borehole and the blocked well log data including a fracture zone inside the Triassic basement (modified after Masri and Takács 2022a)	15
Table 3:	True amplitude data pre-processing sequence with the most important parameters and comments (modified after Masri and Takács 2022a)	20
Table 4:	The most beneficial steps of the true amplitude data pre-processing applied prior to the investigated inversion procedures and lithological analysis (modified after Masri and Takács 2022a)	21
Table 5:	Evaluation of the inverted rock physical models obtained in the study area	64

**Abbreviations**

$V_P$	– P-wave propagation velocity
$V_S$	– S-wave propagation velocity
$V_P/V_S$	– P- and S-wave velocity ratio
$S_W$	– Water saturation
$\sigma$	– Poisson’s ratio
$\Delta\sigma$	– Scaled Poisson’s ratio change
$Z_P$	– P-wave acoustic impedance
$Z_S$	– S-wave acoustic impedance
$\rho$	– Density
$\lambda$	– Incompressibility (first Lamé parameter)
$\mu$	– Rigidity (second Lamé parameter)
$\lambda\rho$	– Elastic impedance ( $\lambda*\rho$ )
$\mu\rho$	– Elastic impedance ( $\mu*\rho$ )

## 1. INTRODUCTION

A multiscale geothermal exploration, started in 2012, resulted successful pairs of production and injection wells near to the city of Győr located on the Little Hungarian Plain, a sub-basin of the Pannonian Basin. The first step of the investigations was a reinterpretation of all archived geological, hydrogeological, and 2D seismic data that was available on the study area. The second step was an additional 2D seismic data acquisition, processing, and interpretation along new profiles. The third phase of the exploration was shooting a local 3D seismic survey planned based on the previous data. At the end, all previous information was integrated and interpreted together for picking out target locations for drilling and well logging. This step-by-step exploration (Kovács et al. 2019) became profitable after hitting a deep geothermal reservoir in the carbonate basement with three pairs of production and injection wells by 2018. Former Geological and Geophysical Institute of Hungary (MFGI), Geo-Log Ltd., and PannErgy Plc. were the partners in this successful geothermal exploration.

The high-quality seismic and well log data gave the opportunity to initiate special local investigations. In 2019, former Mining and Geological Survey of Hungary (MBFSZ) started to study the application possibility of the Amplitude Versus Offset (AVO) analysis for geothermal exploration. At this point, in the framework of a long-standing educational cooperation between MBFSZ and University of Miskolc, I was offered to join the methodological development and that was the beginning of my PhD research in this exciting topic.

AVO analysis have been successfully utilized in the hydrocarbon exploration for more than three decades, however their benefits in the geothermal exploration are recognized just recently. Lithology and rock physical parameters are similar for both type of reservoirs, consequently AVO should work not only to detect hydrocarbons; but to indicate hot water bearing porous geological formations. Of course, the depth is very crucial regarding the high temperature. In my PhD dissertation, I intend to call the attention that inversion techniques based on seismic and well log data (for example AVO inversion and Simultaneous Model-based inversion) can be beneficial for the geothermal exploration.

AVO methodology is based on the anomalous behavior of the pre-stack reflected amplitudes observed from fluid bearing rocks. Ostrander (1984) was the first who demonstrated that AVO responses from both the top and base of a porous gas sand show

anomalous (increasing) trends unlike the AVO responses observed from other lithological boundaries showing normal (decreasing) trends. AVO analysis was introduced in the hydrocarbon exploration in the late 80's and after that the number of productive wells increased significantly not only in the Gulf of Mexico (Allen and Peddy 1993) but all around the world. Later, several authors proved that utilizing the pre-stack amplitude variations, AVO also works for fractured carbonate formations to indicate hydrocarbon bearing porous zones (Harvey 1993, Lynch et al. 1997, Li et al. 2003). Parallel with the above studies, the question came up whether AVO can be applied for other lithological investigations beyond the hydrocarbon exploration, for example to estimate rock properties in the depth range of the middle crust (Pratt et al. 1993, Simon 1998). Takács and Hajnal 2000 and Takács et al. 2021 went even deeper and demonstrated the successful utilization of AVO processing focused on the vicinity of the crust-mantle boundary beneath SE Hungary.

After Goodway (2001) discussed detailed relations between the AVO analysis, Lamé parameters, and the lithology; Russell (2006) pointed out the importance of Elastic Impedance inversion for lithology interpretation. The Lamé parameters (incompressibility and rigidity) are much more characteristic for lithology interpretation and porosity detection than the P- and the S-wave velocity parameters, or even their ratio. The new seismic tool (Simultaneous Model-based inversion) based on the joint inversion of pre-stack reflected P- and S-wave amplitudes, was added to the toolbox of hydrocarbon exploration.

In the last decade, only a few authors studied the benefits of AVO analysis for geothermal exploration, however the number of publications is growing in this topic. Aleardi and Mazzotti (2012) investigated a geothermal reservoir located in the fractured intrusive basement of the Larderello-Travale geothermal field, Italy. They concluded that AVO responses from the fractured zones of massive basement can be different from the well-known amplitude responses of clastic sediments. The authors declared that „we need to derive a new AVO attribute which may highlight fracture locations in this peculiar rock type”. Russell (2020) underlined the potential of AVO inversion and analysis in the geothermal exploration and concluded that adaptation of the methodology can be very promising for geothermal reservoir development. Recently, Allo et al. (2021) published their study on the utilization of neural networks in the characterization of a carbonate geothermal reservoir located in the Paris Basin, France.

## 2. AVO THEORY

AVO procedure applies true amplitude processed pre-stack seismic data analyzing the reflected P-wave amplitude as a function of the source-receiver offset (or incident angle). The offset–angle conversion of the CDP gathers is performed utilizing the velocity measurement of the available sonic logs or the velocity field obtained by seismic velocity analysis (Hampson-Russell Software Services Ltd. 2004). The rock physical parameters P- and S-wave velocities ( $V_P$  and  $V_S$ ) and density ( $\rho$ ) above and below the seismic interfaces can be obtained by a robust inversion algorithm (conjugate gradient method). One of the advantages of the AVO inversion process is that direct S-wave recording is not necessary to get S-wave velocity information, it is calculated from the P-wave observations. On the other hand, after the calculations, several other useful elastic parameters can be derived. The derived parameters are the velocity ratio ( $V_P/V_S$ ), the Poisson's ratio ( $\sigma$ ), and two another elastic parameters related to the Lamé parameters ( $\lambda$ – incompressibility and  $\mu$ –rigidity). This rock physical parameter set is very helpful for lithology discrimination and porosity detection in any study area.

### 2.1. Brief historical overview

In the late 1960s, the ‘bright spot technology’ resulted in several dry hydrocarbon exploration wells in the Gulf of Mexico. The reason was that high energy reflections (bright spots) can be caused not only by hydrocarbon content but also by other reasons, for instance magmatic or coal layers or even by the thin layer effect (Chopra and Castagna 2014). In the late 1970s, a more detailed analysis of the Direct Hydrocarbon Indicators (bright spots, flat spots, dim spots, polarity change, high frequency attenuation) observed in the seismic sections resulted in more success in the hydrocarbon exploration. The methodology became available after Taner's et al. (1979) publication when they introduced the term of ‘complex seismic trace’. Calculation of the reflection strength, instantaneous phase and polarity, and apparent frequency attributes based on the Hilbert-transformation didn't require high-capacity computers; and they were computed directly from the post-stack migrated seismic traces without utilizing any well log data.

In the same year, another methodology was published by Lindseth (1979) to obtain P-wave acoustic impedance data from the reflected amplitudes of the post-stack seismic traces.

This procedure became known as ‘SEISLOG technique’ and turned into a prevalent tool in the hydrocarbon exploration. The process utilized not only the post-stack seismic data but also used well log information (in-situ sonic and density data) to build up initial model for the subsequent inversion process. This point can be regarded as the beginning of a new approach which was labelled as Seismic Lithology.

The next step towards an even more reliable lithology (and porosity) estimation was Ostrander’s (1984) fundamental publication. He proved that amplitude variations of the reflected signals with the source-receiver offset observed in the pre-stack CDP gathers were sensitive for the gas content of clastic sediments showing an anomalous behavior (increasing amplitudes with the increasing offset). After introducing Amplitude Versus Offset (AVO) analysis into the hydrocarbon exploration, the number of productive wells increased significantly, and the method was introduced worldwide. There was a debate in the geophysical community whether AVO could work for fractured carbonates too (and not only for clastic sediments); but several authors proved that with successful case studies (such as Harvey 1993, Linch et al. 1997, and Li et al. 2003). Finally, utilization of the AVO attributes (Intercept, Gradient, Product, Fluid Factor, and Scaled Poisson’s Ratio Change) became reliable tools of the hydrocarbon indicators. Beyond the pre-stack seismic data, AVO inversion also requires well logs (sonic and density, and Full Wave Sonic at best). It needs very careful true amplitude seismic data processing before the inversion and lithological interpretation, and much higher computing power than the above-mentioned Hilbert and SEISLOG algorithms do.

Goodway (2001) was the first who pointed out the importance of Lamé constants (incompressibility and rigidity) in lithology discrimination and porosity detection, and Russell and Hampson (2006) foreseen the possibility to estimate them from the pre-stack seismic amplitudes. To estimate the Lamé constants, we must perform a complex pre-stack workflow starting with AVO inversion, proceeding with the simultaneous inversion of P- and S-wave acoustic impedances and the density; and finally getting rock physical parameters related to the incompressibility and rigidity. I intend to prove that the above workflow can be utilized not only for the hydrocarbon industry but also for the geothermal exploration. The reason is that the lithological model (fluid saturated porous geological formation) and its rock physical properties are very similar. In the next chapters, I will give a summary around the rock

physical basics, the Biot-Gassmann theory, and the Zoeppritz equations with their practical approximations.

## 2.2. Rock physical basics

Amplitude Versus Offset (AVO) response of any porous reservoir depends on its P- and S-wave velocity ( $V_P$  and  $V_S$ ), and density ( $\rho$ ) parameters – involving the matrix material, the pore space, and the fluid fills in the pores. A common way to look the relation between  $V_P$  and  $V_S$  in reservoir exploration is given by the Poisson's ratio ( $\sigma$ ):

$$\sigma = (V_P^2 - 2V_S^2)/2(V_P^2 - V_S^2).$$

Poisson's ratio depends on the solid-rock material, the volume and shape of the pore space, and the fluid saturation (Chopra and Castagna 2014). Since the rock material is dependent on the mineral composition, it influences the Poisson's ratio (Fig. 1). It is also important to note that in case of two-phase fluid saturated rocks (gas and water), the Poisson's ratio is decreasing with increasing gas content (Fig. 2). The presence of only a very few amounts of gas in the pores will significantly decrease the  $V_P/V_S$  ratio and consequently the Poisson's ratio ( $\sigma$ ). The reason is that P-wave velocity drops very suddenly even in the presence of a small amount of gas content, but S-wave velocity does not change significantly because it does not travel in fluids, it travels only in the rock matrix.

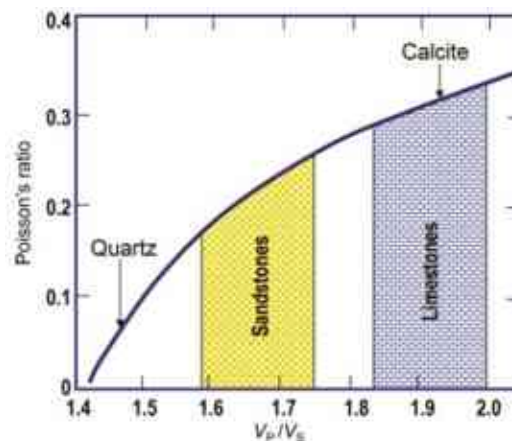


**Fig. 1**  $V_P/V_S$  and Poisson's ratio for different rocks and mineral types (Chopra and Castagna 2014)

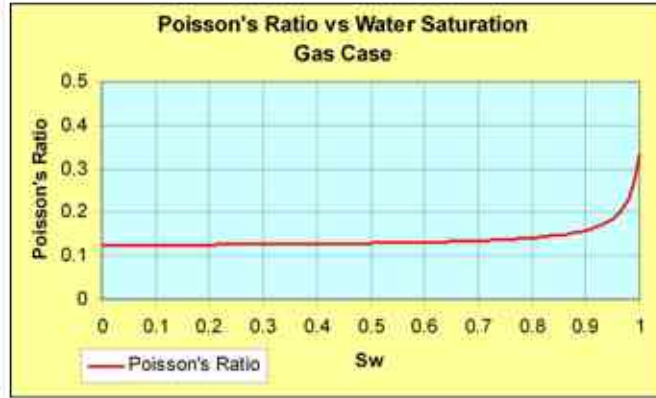


**Fig. 2** Poisson’s ratio versus water saturation ( $S_w$ ) for a two-phase water and gas model (Hampson-Russell Software Services Ltd. 2009). Note that any fluid content lowers the Poisson’s ratio of any porous rock compared with the solid rock (Chopra and Castagna 2014).

### 2.3. Biot-Gassmann theory

Gassmann (1951) and Biot (1956) established independently their developments for the wave propagation in fluid saturated rocks (Fig. 3). They derived expressions for the saturated bulk ( $K$ ) and shear ( $\mu$ ) moduli and applied them in the regular equations of wave velocities ( $V_P$  and  $V_S$ ):

$$V_{P_{sat}} = \sqrt{\frac{K_{sat} + \frac{4}{3}\mu_{sat}}{\rho_{sat}}} \quad \text{and} \quad V_{S_{sat}} = \sqrt{\frac{\mu_{sat}}{\rho_{sat}}} \quad \text{where } \rho \text{ is the density.}$$

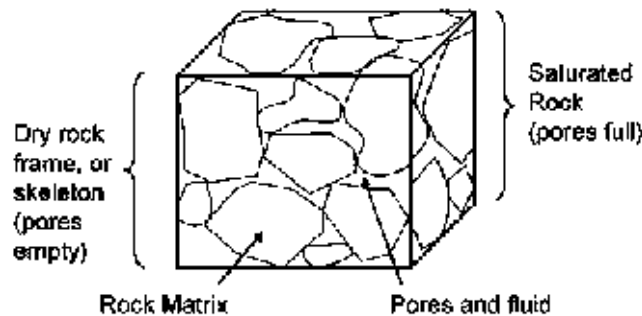


**Fig. 3** Rock components: skeleton, pores, and fluid (Hampson-Russell Software Services Ltd. 2009)

In the Biot-Gassmann equation, the shear modulus does not change with varying fluid saturation at a constant porosity ( $\mu_{sat} = \mu_{dry}$ ) and the bulk modulus is defined as follows:

$$K_{sat} = K_{dry} + \frac{\left(1 - \frac{K_{dry}}{K_m}\right)^2}{\frac{\phi}{K_{fl}} + \frac{1-\phi}{K_m} - \frac{K_{dry}}{K_m^2}}$$

where ‘sat’ distinguishes the saturated rock, ‘dry’ the dry rock, ‘m’ the rock matrix, ‘fl’ the fluid, and  $\phi$  is the porosity. A rearranged version of the above equation provides a more instinctive formula by Mavko et al. (1998):

$$\frac{K_{sat}}{K_m - K_{sat}} = \frac{K_{dry}}{K_m - K_{dry}} + \frac{K_{fl}}{\phi (K_m - K_{fl})}$$

The bulk modulus of the solid rock matrix ( $K_m$ ) is usually taken from published data measured on drill core samples. The typical value for sandstones is 40 GPa and it is 60 GPa for limestones. The bulk modulus for the fluid fill can be calculated by the following relation obtained from the volume average equation:

$$\frac{1}{K_{fl}} = \frac{S_w}{K_w} + \frac{1-S_w}{K_{hc}}$$

where  $K_{fl}$  is the bulk modulus of the fluid,  $K_w$  is the bulk modulus of the water,  $K_{hc}$  is the bulk modulus of the hydrocarbon, and  $S_w$  is the water saturation. The above presented Biot-Gassmann equations provide a good understanding of the rock physical properties of fluid saturated geological formations.

## 2.4. Zoeppritz equations and their approximations

Theoretical studies of the reflection and transmission coefficients were provided by Zoeppritz (1919) to determine the amplitude variations of the reflected and transmitted P- and S-waves with the incident angle at a single seismic interface for the entire range of incident angles (between 0° and 90°). In case of an incident P-wave, the equation is written as follows:

$$\begin{bmatrix} R_P \\ R_S \\ T_P \\ T_S \end{bmatrix} = \begin{bmatrix} -\sin\theta_1 & -\cos\phi_1 & \sin\theta_2 & \cos\phi_2 \\ \cos\theta_1 & -\sin\phi_1 & \cos\theta_2 & -\sin\phi_2 \\ \sin 2\theta_1 & \frac{V_{P1}}{V_{S1}} \cos 2\phi_1 & \frac{\rho_2 V_{S2}^2 V_{P1}}{\rho_1 V_{S1}^2 V_{P2}} \sin 2\theta_2 & \frac{\rho_2 V_{S2} V_{P1}}{\rho_1 V_{S1}^2} \cos 2\phi_2 \\ -\cos 2\phi_1 & \frac{V_{S1}}{V_{P1}} \sin 2\phi_1 & \frac{\rho_2 V_{P2}}{\rho_1 V_{P1}} \cos 2\phi_2 & \frac{\rho_2 V_{P2}}{\rho_1 V_{P1}} \cos 2\phi_2 \end{bmatrix}^{-1} \begin{bmatrix} \sin\theta_1 \\ \cos\theta_1 \\ \sin 2\theta_1 \\ \cos 2\phi_1 \end{bmatrix}$$

where R and T are the reflection and transmission coefficients,  $V_P$ ,  $V_S$ , and  $\rho$  are the P- and S-wave velocities and the density, while  $\theta$  and  $\phi$  mark the angles of incidence, reflection, and transmission for the generated P- and S-waves (Fig. 4).

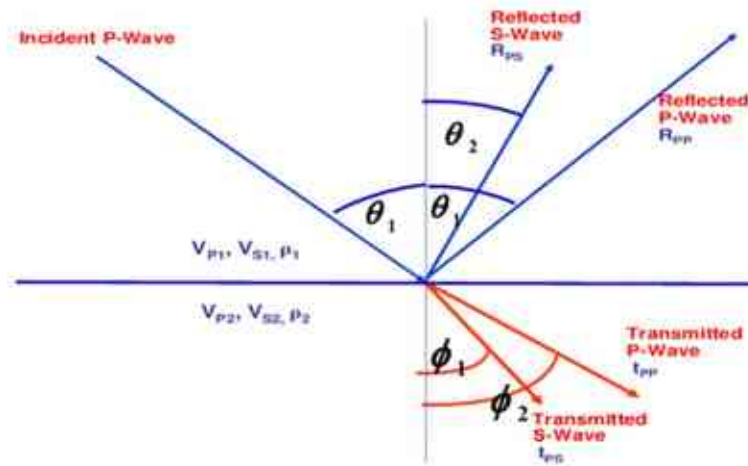


**Fig. 4** Elastic waves generated at a single interface in case of incident P-wave (modified after Takács et al. 2021)

In practice, several simplifications of the above matrix equation are applied to perform AVO inversion on the reflected P-wave data. The most popular ones are the Aki-Richards and the Shuey's equations (Richards and Frasier 1976, Shuey 1985). Those approximations work properly in the range of incident angles that usually can be observed by a regular surface seismic survey.

Based on Aki-Richard's theory (in the range of  $0^\circ$ – $40^\circ$ ), the reflection coefficient (R) can be calculated by a three-term function of the incident angle ( $\theta$ ) at a single seismic interface:

$$R(\theta) = A + B \sin^2\theta + C \sin^2\theta \tan^2\theta$$

where the constants can be expressed as

$$A = \frac{1}{2} \frac{\Delta(\rho\alpha)}{(\rho\alpha)} = \text{Intercept}, B = \left( \frac{1}{2} \frac{\Delta\alpha}{\alpha} - 4 \frac{\beta^2 \Delta\beta}{\alpha^2 \beta} - 2 \frac{\beta^2 \Delta\rho}{\alpha^2 \rho} \right) = \text{Gradient}, \text{ and } C = \frac{1}{2} \frac{\Delta\alpha}{\alpha} = \text{Curvature}$$

while  $\theta$  is the incident angle,  $\alpha$  is the P-wave velocity,  $\beta$  is the S-wave velocity, and  $\rho$  is the density of the lithological formation. According to Shuey’s approach (in the range of  $0^\circ$ – $30^\circ$ ), the third term  $C$  (Curvature) can be neglected, thus his approximation resulted in a simple linear function with the two very basic AVO attributes called A–Intercept and B–Gradient (Fig. 5):

$$R(\theta) = A + B \sin^2\theta \tag{1}$$

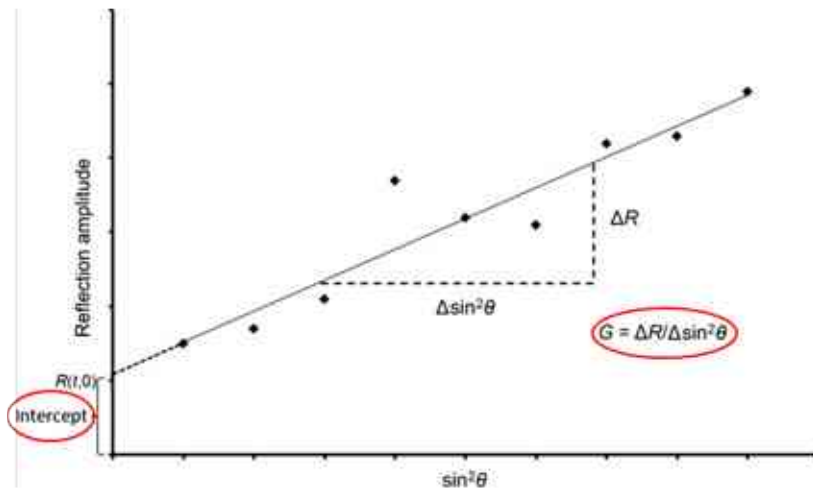


**Fig. 5** Linear regression of the observed pre-stack amplitudes with the square of sin of incident angle defining the two basic AVO attributes (Intercept and Gradient) at a time sampling location of a CDP gather (after Chopra and Castagna 2014)

It must be noted that the AVO attribute ‘Intercept’ is related to the zero-offset reflection coefficient and the ‘Gradient’ is very sensitive for the porosity and fluid content. At the beginning of AVO application in the hydrocarbon industry (in the late 80’s), the two basic

attributes were successfully applied in the mapping of porous zones. Later, other sophisticated procedures based on the above described AVO theory, were worked out for the estimation of more practicable rock physical properties (Goodway 2001, Russell 2006) with more physical meaning. Those advanced techniques will be presented in the next part of my dissertation.

## **2.5. Examples for normal and anomalous AVO responses in clastic sediments**

Lithological boundaries, in most cases, generate decreasing (normal) AVO responses but some of them produce increasing (anomalous) trends. In Fig. 6, a normal amplitude response is presented that usually can be observed from a boundary located between solid geological formations (with no porosity). In Fig. 7, an anomalous AVO response is demonstrated that usually can be detected from a boundary located between solid and fluid saturated porous rocks. At this point, it is important to define the terms of ‘decreasing’ and ‘increasing’ AVO trends.

Decreasing and increasing amplitude trends in AVO analysis are defined regarding the absolute values (or the energy) of the reflected amplitudes. Thus, the amplitude variation with offset is obviously decreasing in Fig. 6 because positive amplitudes are decreasing with the increasing offset (the reflection coefficient is positive). However, the amplitude variation presented in Fig. 7 is increasing because the negative amplitudes (considering their absolute values) are increasing with the increasing offset (the reflection coefficient is negative). The offset dependent reflectivity modelling was carried out with the utilization of the exact solution of the above Zoeppritz’s matrix equation (Young and Braile 1976).

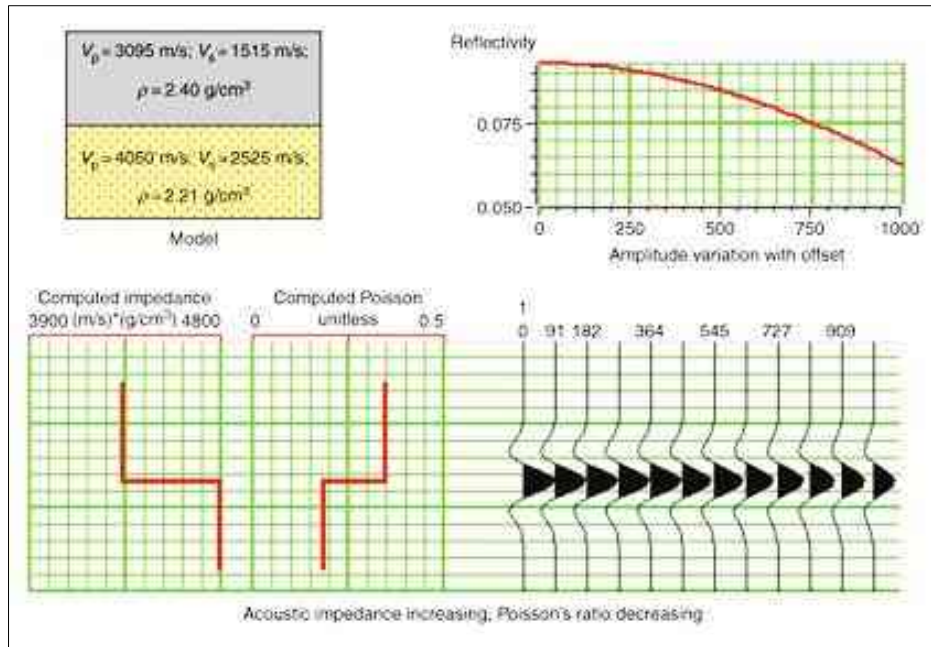


**Fig. 6** Normal AVO response (modified after Chopra and Castagna 2014). This model represents an interface between solid rocks. Note that the zero-offset reflection coefficient is a positive value thus the AVO response is considered as a decreasing trend because the reflected energy is decreasing with the offset.

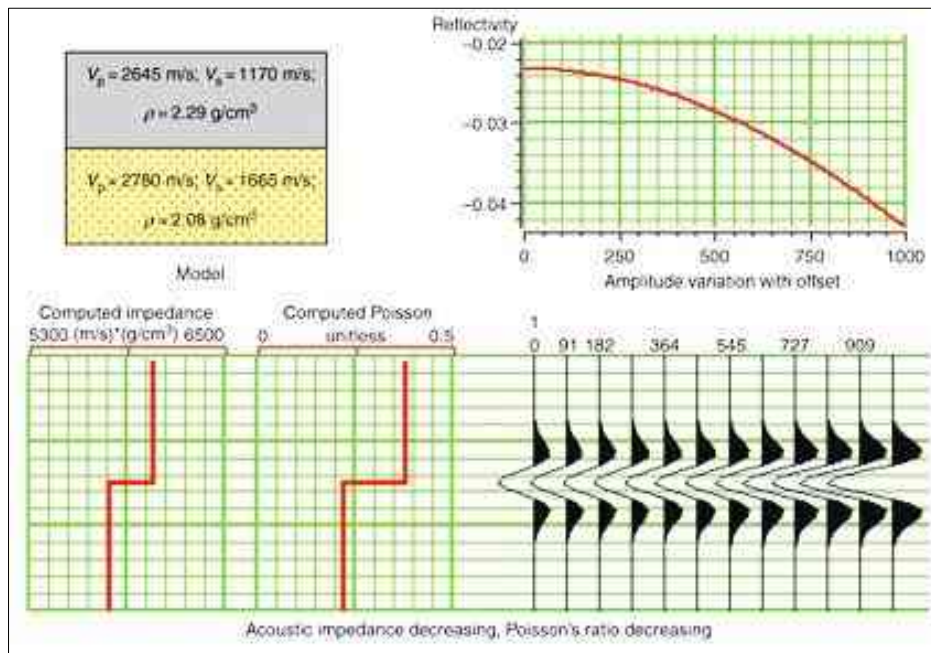


**Fig. 7** Anomalous AVO response (modified after Chopra and Castagna 2014). This model represents an interface between solid and porous rocks. Note that the zero-offset reflection coefficient is a negative value thus the AVO response is considered as an increasing trend because the reflected energy is increasing with the offset.

### 3. GEOLOGICAL FRAMEWORK AND GEOPHYSICAL DATASET

Geological, geothermal, and geophysical information around my study area will be summarized in this chapter.

#### 3.1. Background geology and available geophysical data

The study area (Fig. 8) is in the Hungarian part of the Danube Basin, which is the northwestern sub-basin of the Pannonian Basin (Sztanó et al. 2016). The sub-basin is characterized by vertical and lateral movements, pervasive extensional faulting, and high sandstone content in the Neogene sequence (Dolton 2006). Basement traps at the base Cenozoic include paleo-topography, truncations, and local porosity zones in the fractured and fissured traces of shear zones. In the western and northwestern part of the Danube Basin, the basement is dominated by high-grade metamorphic rocks. The Transdanubian Range, constituting the basement in the eastern and southeastern part of the Danube Basin, however, has only low-grade metamorphics and is dominated by various Mesozoic carbonate successions (Tari 1994, Fodor et al. 2003, Tari and Horváth 2010). The limit of the Transdanubian Range to the NW is the Rába Fault zone, a Miocene detachment fault system.

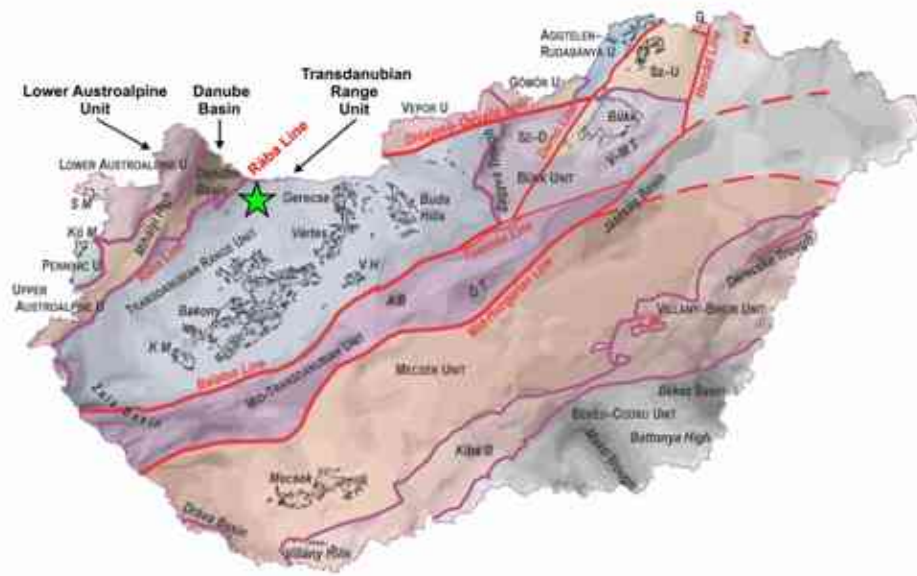


**Fig. 8** Location map showing the pre-Cenozoic geology structure of Hungary (modified after Haas et al. 2014) and the scope of the area of investigation marked with the green star

The geothermal gradient, and consequently the heat flow, is very high beneath the Danube Basin of the Pannonian Basin System (Békési et al. 2018). In the area of investigation, located on the northwest flank of the Transdanubian Range, productive geothermal wells with higher effluent temperature than 100 °C can be expected only if they hit the basement (Cserkész-Nagy et al. 2020). The above described geological and geothermal settings provide an excellent environment for the exploration of hot water bearing reservoirs, mainly in the deeper parts, especially in the carbonate rocks of the pre-Cenozoic basement. Table 1 summarizes the geology and lithology revealed by a productive geothermal well located on the area of investigation.

**Table 1** Geology and lithology in a productive geothermal well of the study area (modified after Masri and Takács 2022a). Vertical depth values are not indicated by confidentiality reason.

<b>Geology and lithology in the productive well</b>	<b>Markers (tops) shown in the presented attribute sections</b>
<b>Pliocene</b> claystone	<b>PL1_E</b>
<b>Miocene</b> sandy claystone, claystone with aleurolite, claystone	<b>M</b>
<b>Miocene</b> clay marl	<b>M1</b>
<b>Miocene</b> clay marl, aleurolite, sandstone strips	<b>M2</b>
<b>Triassic</b> clay marl, friable dolomite, dolomite	<b>T</b>
<b>Triassic</b> hot water saturated fractured dolomite	<b>FR and/or PR</b>
<b>Triassic</b> calcareous marl	<b>T1</b>

Limited selection of well logs was available in the above well, including measured sonic log which was essential to estimate P-wave impedance data at the location of the hole.

Unfortunately, neither S-wave velocity (Full Wave Sonic) nor density logging was carried out in this hole penetrated deep inside the Triassic basement.

In my dissertation, I investigated a 2 x 2 km portion of a larger 3D seismic dataset that was pre-processed utilizing true amplitude data processing to obtain reliable lithology information based on the reflected amplitudes. Cropping the available larger seismic volume was necessary to save running time for the time-consuming pre-stack Kirchhoff migration to get appropriate input data for the lithological analyses. In the next chapters, I will present the results of my AVO modelling and the rock physical models obtained by different kinds of subsequent inversion processes focusing on the above discussed geothermal reservoir located in the Triassic basement.

#### **4. MODELLING AND DATA PREPARATION**

Modelling the probable AVO responses of the study area and a careful preparation of all the available data sometimes takes more time than the AVO inversion and analysis.

##### **4.1. AVO modelling based on well log data**

Before starting a reliable AVO inversion and analysis, an important step is the modelling (Masri and Takács 2022a). I calculated theoretical AVO responses to study whether the fluid saturated porous rocks (hot water bearing fractured zones in the Triassic carbonate basement) can cause any AVO anomaly. The lithological model and its rock physical parameters obtained from well log data is presented in Table 2 where the hot water bearing fractured zone with a thickness of about 60 m is highlighted with the row colored by green.

**Table 2** Seven-layer-model based on the borehole and the blocked well log data including a fracture zone inside the Triassic basement (modified after Masri and Takács 2022a). Depth values are not indicated by confidentiality reason.

Geology and lithology	Top name	Rock physical parameters between the tops			
		V <sub>P</sub> [m/s]	V <sub>S</sub> [m/s]	σ [unitless]	ρ [g/ccm]
<b>Pliocene</b> claystone	<b>PL1_E</b>	3118	1503	0.349	2.32
<b>Miocene</b> sandy claystone, claystone with aleurolite, claystone	<b>M</b>	3360	1702	0.327	2.36
<b>Miocene</b> clay marl	<b>M1</b>	3246	1615	0.336	2.34
<b>Miocene</b> clay marl, aleurolite, sandstone strips	<b>M2</b>	3629	1944	0.299	2.41
<b>Triassic</b> clay marl, friable dolomite, dolomite	<b>T</b>	5149	3260	0.166	2.63
<b>Triassic</b> hot water saturated fractured dolomite	<b>FR and/or PR</b>	4934	3218	0.130	2.60
<b>Triassic</b> calcareous marl	<b>T1</b>	4623	2810	0.207	2.56

Resistivity, P- and S-wave velocity, and density logs obtained from the deviated productive well (after applying 11-point median filter) are displayed in Fig. 9. It must be noted that only the resistivity and P-wave velocity (sonic) logs were measured in the well, the S-wave velocity and density logs were calculated based on the Castagna et al. (1985) and the Geertsma and Smit (1961) equations. The correlation between the measured resistivity (blue) and P-wave (red) logs is excellent and both calculated logs (orange) show the expected low values inside the fractured zone between the green markers of FR and T1 (top and base of the fractured zone). The decreasing values beneath the T1 marker are explained with the presence of Triassic calcareous marl drilled down to the end of hole (see Table 1).

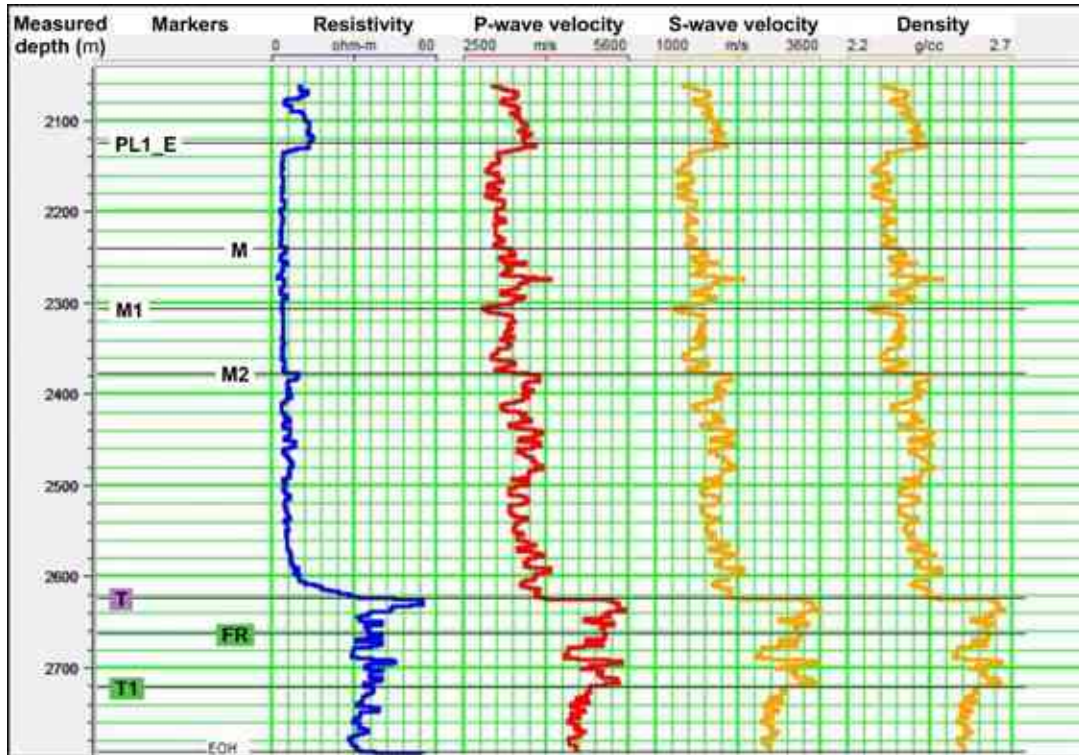


**Fig. 9** Logs from a productive deviated geothermal well along the well trajectory (modified after Masri and Takács 2022a). Blue and red logs: measured resistivity and P-wave velocity; yellow logs: calculated S-wave velocity and density. Magenta T marker denotes the top of the Triassic basement. Green FR and T1 markers show the top and base of the fractured zone inside the basement.

Blocked rock physical parameters ( $V_P$ ,  $V_S$ ,  $\sigma$ , and  $\rho$ ), obtained from the above well logs and utilized for the subsequent AVO modelling, are demonstrated in Fig. 10. Note that the Poisson's ratio ( $\sigma$ ) value of 0.13 for the fractured zone (between the markers FR and T1) was set up considering high formation pressure in the investigated water saturated carbonate basement. That high pressure can make the rock matrix weak and decrease the S-wave velocity ( $V_S$ ) significantly. The calculated zero-offset reflectivity (magenta series) and the Zoeppritz synthetics (demonstrated by black traces) are also presented in the figure. The synthetic traces show the variations of the theoretical reflected amplitudes within the range of incident angles between 0 and 40 degrees. A characteristic anomalous effect in the wave field, caused by the hot water saturated fractured zone, is clearly seen inside the green ellipse. In other words, the reflection coefficient has a polarity change within the incident angle range (0-40°).

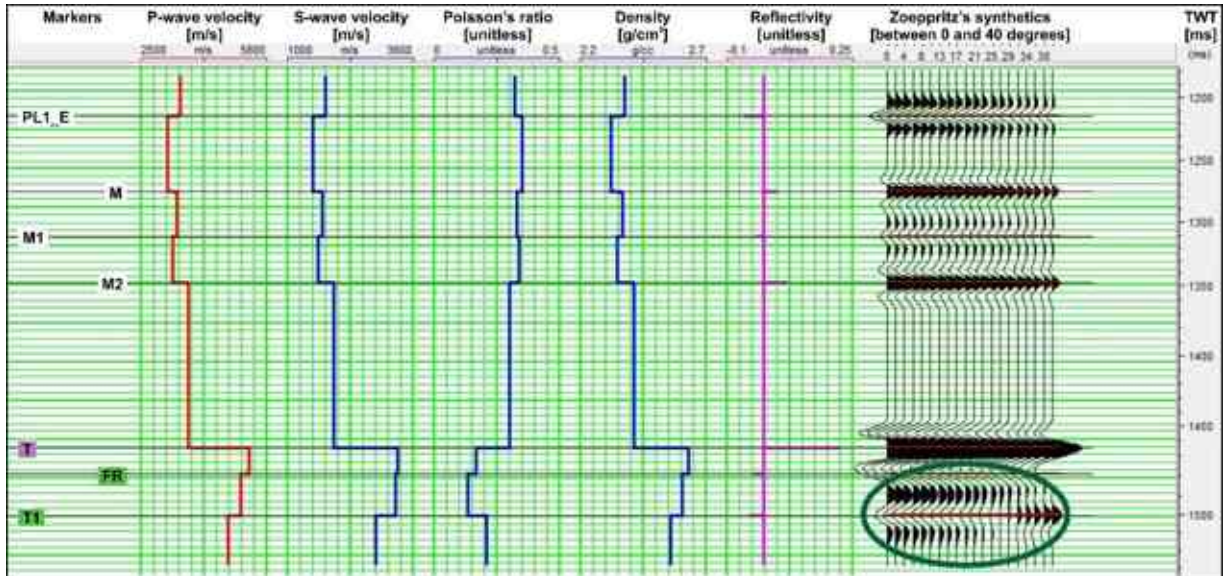


**Fig. 10** Model parameters after blocking the well logs (modified after Masri and Takács 2022a). Domain: two-way-time. Red curve: P-wave velocity; blue curves: S-wave velocity, Poisson's ratio, and density. Magenta series: zero-offset reflectivity. Zoeppritz synthetics (black traces) as functions of the incident angle show significant anomaly in the wave field between the FR and T1 markers.

A more detailed insight is provided in Fig. 11 showing all theoretical AVO responses of the above model. Based on those seismic responses, we can say that only the light green AVO curve generated from the base of the hot water saturated dolomitic fractured zone (T1) shows anomalous behavior compared with the other responses. It has a negative intercept (zero-offset reflection coefficient), and very importantly an 'angle of crossover' less than 25 degree. These peculiar features distinguish this AVO response from the other ones. Thus, for mapping the hot water bearing deep fractured zone in this study area, a combination of the intercept and the 'angle of crossover' as a new AVO attribute might be a helpful indicator beside the earlier mentioned conventional ones (A-Intercept and B-Gradient).

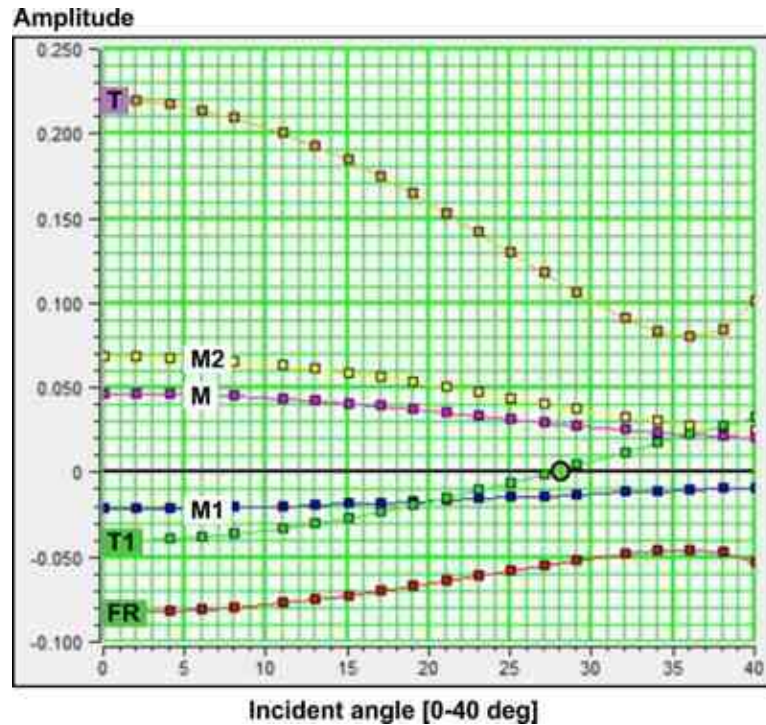


**Fig. 11** Theoretical AVO responses from the interfaces of the above discussed seven-layer-model (modified after Masri and Takács 2022a). The presented curves correspond with the markers explained in Tables 1 and 2. Note the light green anomalous trend (T1) generated from the bottom of the fracture zone having an angle of crossover less than 30°.

➤ **Thesis 1** on the AVO modelling:

I proved that AVO response of a geothermal reservoir located in the fractured carbonate basement can be very different from the usual response of any gas sands located in clastic sediments. Both the top and the base of a clastic gas sand usually have increasing AVO responses. I built up a seven-layer rock physical model based on the well log data of my study area (Little Hungarian Plain) and demonstrated that the AVO response of the investigated Triassic geothermal reservoir had peculiar characteristics. On the one hand, AVO responses both from the top and the base of the dolomite fracture zone show decreasing amplitudes with the offset (incident angle). On the other hand, the AVO responses from the base of the investigated fractured reservoir show anomalously low angle of crossover (less than 30°) together with negative intercept value (zero offset reflection coefficient). For this reason, introduction of a new AVO attribute, combination of angle of crossover and intercept, would be helpful for geothermal investigations in case of exploration of the deep dolomite basement.

#### 4.2. True amplitude seismic data pre-processing

During a surface seismic survey, amplitude and phase properties of the reflected signals are altered by many factors. Those effects are caused by the source and the environment (air wave, surface wave, ground roll, and human activity in the deployment), by the observation (differences in the coupling of sources and receivers), or simple by the physical effects of wave propagation (energy losses). The objective of the true amplitude data processing is to get reflection signals that are free from those effects and provide us with the best possible image of the subsurface for quantitative interpretation. This objective can be accomplished by the correction of the above-mentioned harmful effects.

Subsequent AVO examinations require very careful data pre-processing known as 'true amplitude', 'relative amplitude', or 'amplitude preserved' data processing. All these terms refer to the same points. On the one hand, we must take every effort to restore the relative trace-by-trace amplitude variations of the reflected signals applying certain special data processing steps (for example true amplitude recovery and surface consistent procedures). On the other hand, to obtain quantitative information from the reflected amplitudes, we must avoid any processing step that can distort the relative amplitudes of the individual traces (for example Automatic Gain Control or Trace Equalization). The input data for AVO inversion and analysis is a set of the true amplitude processed, NMO (Normal Move-Out) corrected, pre-stack migrated CDP (Common Depth Point) gathers (Mazzotti and Mirri 1991, Mazzotti and Ravagnan 1995, Chopra and Castagna 2014). To obtain those gathers, we must recover the relative amplitudes of the reflections which had been distorted by the data acquisition and wave propagation. Also, we must avoid any data processing step which can change the trace-by-trace amplitudes. In this way, we can get appropriate CDP gathers with reliable relative amplitude variations (AVO responses) that are related only with the changes of lithology and/or fluid content.

The next procedure, after the above discussed careful seismic data pre-processing, is the calculation of AVO attributes utilizing the input CDP gathers and the well logs available in the study area. AVO attributes are very helpful in porosity indication, and the most popular ones are the so-called Product and Scaled Poisson's Ratio Change (Chopra and Castagna 2014). They can be derived from the two basic attributes Intercept and Gradient which were defined in Fig. 5. In Chapter 5.2, I will discuss those derived attributes in detail, and I will

present a practical example from my study area to show the benefits of the Scaled Poisson’s Ratio Change AVO attribute for porosity detection.

Considering the above requirements, the following pre-processing sequence (Table 3) was applied on the 3D seismic data with the help of the former Mining and Geological Survey of Hungary (MBFSZ) utilizing their ProMAX software (Landmark Graphics Corporation 2001). That was the beginning of my PhD investigation on real seismic data.

**Table 3** True amplitude data pre-processing sequence with the most important parameters and comments (modified after Masri and Takács 2022a)

Data processing step	Most important parameters and comments
1. Bandpass Filtering	12-16-60-65 Hz, notch filter: 50 Hz
2. True Amplitude Recovery (TAR)	See <b>Table 4</b> for the aim and effect
3. Trace Editing (KILL, MUTE)	Trace Editing was carried out formerly when the data was processed for conventional imaging (2014)
4. Surface Consistent Amplitude Balancing	See <b>Table 4</b> for the aim and effect
5. Air Blast Attenuation	Attenuated velocity range: 200-700 m/s (in 50 m/s steps), filter to enhance air blast: 10-15-25-30 Hz
6. Surface Consistent Deconvolution	See <b>Table 4</b> for the aim and effect
7. Bandpass Filtering	12-16-60-65 Hz
8. Refraction Statics	Refraction Statics were calculated formerly when the data was processed for conventional imaging (2014)
9. Velocity Analysis	Velocity Analysis was carried out formerly when the data was processed for conventional imaging (2014)
10. Residual Statics	Time Varying Trim Statics using a sliding window with 400 ms length
11. Kirchhoff PSTM Migration	See <b>Table 4</b> for the aim and effect

From the viewpoint of quantitative interpretation, I summarized the most beneficial steps of the above true amplitude seismic data pre-processing sequence in Table 4.

**Table 4** The most beneficial steps of the true amplitude data pre-processing applied prior to the investigated inversion procedures and lithological analysis (modified after Masri and Takács 2022a)

Data processing step	Aim and effect
True Amplitude Recovery (TAR)	Correction of the amplitude attenuation caused by the wave propagation (spherical divergence)
Surface Consistent Amplitude Balancing	Correction of the amplitude variations caused by the changing field survey conditions (variable source and receiver coupling)
Surface Consistent Deconvolution	Correction of the waveform variation caused by the changing field survey conditions (variable source and receiver coupling)
Kirchhoff Pre-stack Time Migration with Normal Move-out (NMO) correction	Removes the diffractions caused by sharp structural changes (for example fault edges and pinch out structures) that distort the reflected amplitudes. NMO correction removes the geometrical effect (flattens the reflection hyperbolas).

The next step was importing the properly pre-processed seismic data into the Hampson-Russell AVO software (Hampson-Russell Software Services Ltd. 2009), where the available well logs of the study area have had been loaded and the AVO modelling was performed earlier. Hampson-Russell AVO package provided me two more processing steps to enhance the coherency of the imported CDP gathers (applying trim static corrections and creating super gathers). I will demonstrate the additional coherency improvements in the next figures (Figs. 12, 13, and 14).

The blue horizon marked in the CDP gathers presented below denotes the previously estimated top of the fractured geothermal reservoir based on the conventional migrated stack volume. This horizon must be differentiated from the dotted horizons that I will present later as the top of the Triassic basement based on the inverted rock physical models (Figs. 31, 32, 33, and 34). The top of the reservoir will be detected in a more sophisticated way by the results of the inversion processes discussed in Chapter 5.

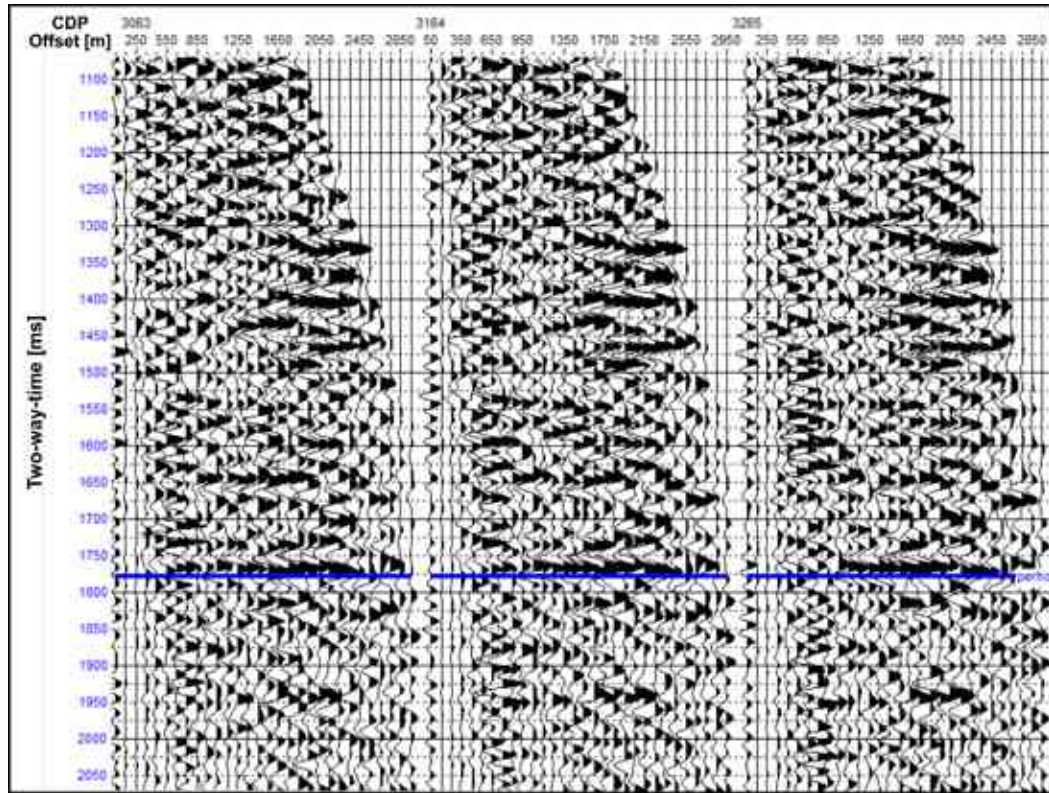


**Fig. 12** CDP gathers close to the location of a productive geothermal well (see Fig. 19). The pre-processed seismic data was imported from the ProMAX into the Hampson-Russel AVO software. The blue horizon marks a preliminary estimated top of the Triassic reservoir as interpreted in 2006 based on the migrated 3D stack volume.

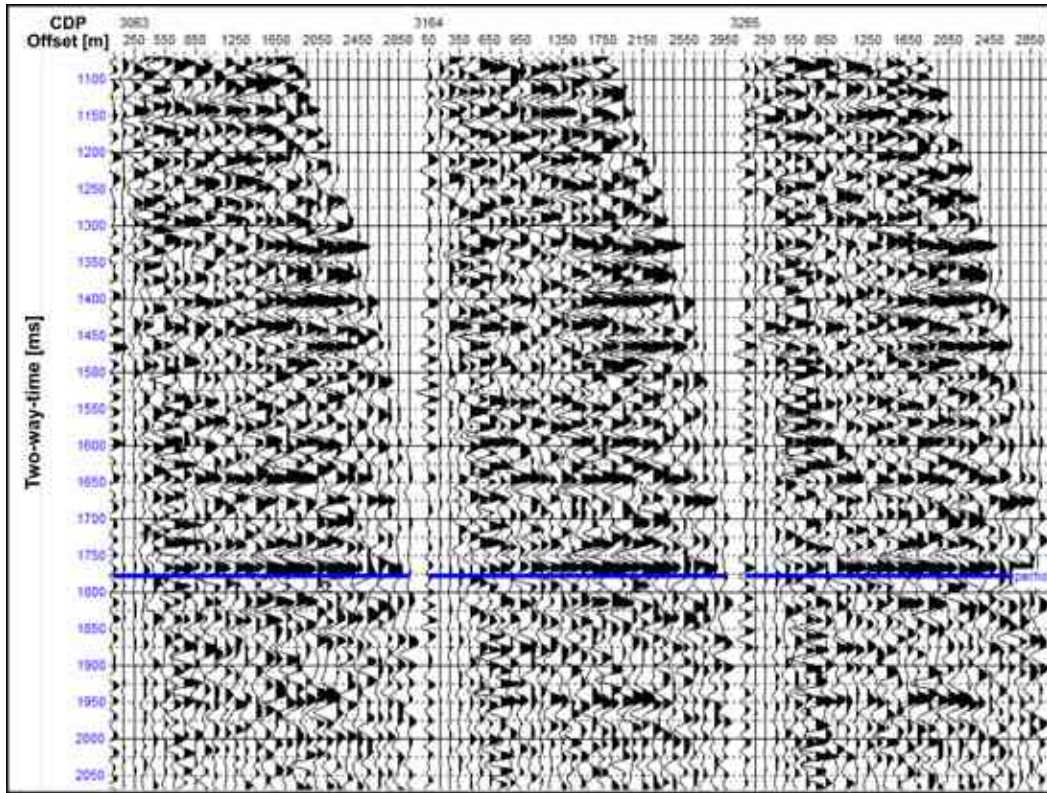


**Fig. 13** CDP gathers after applying trim static corrections in the Hampson-Russell AVO software utilizing the blue horizon. The blue horizon is explained in the caption of Fig. 12.

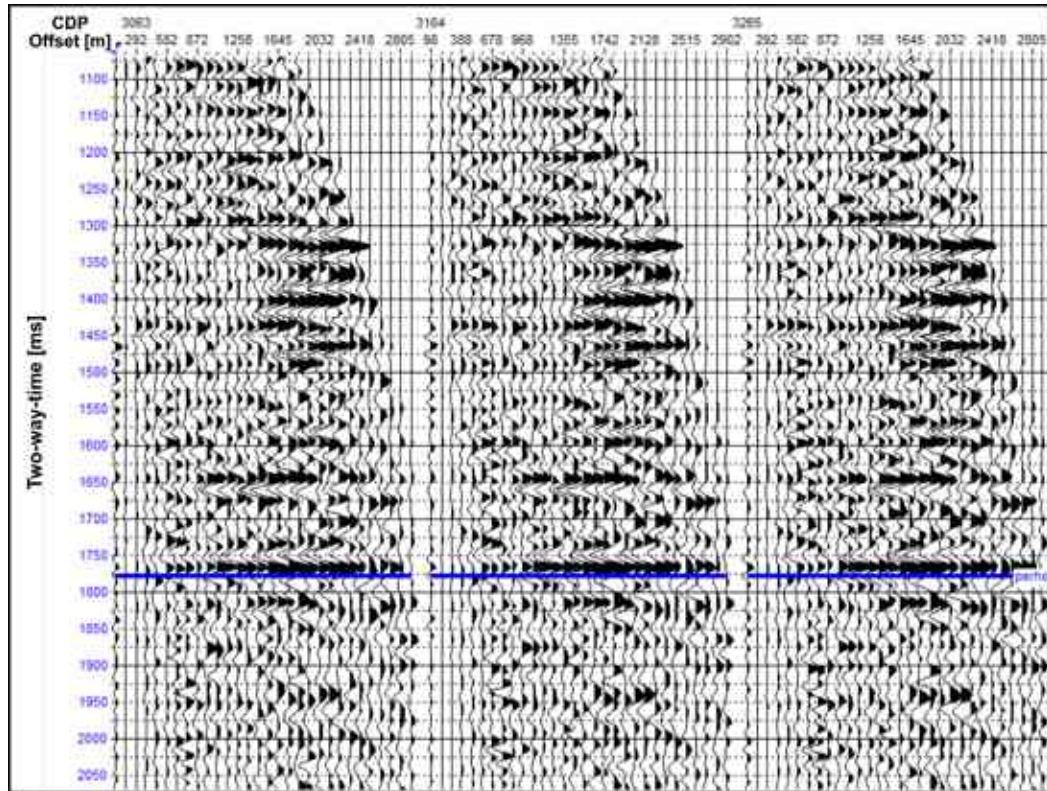


**Fig. 14** CDP super gathers after vertical stacking of five adjacent individual CDPs obtained by the earlier application of trim static corrections. Vertical stacking means a stack of the seismic traces having the same source-receiver offset. The blue horizon is explained in the caption of Fig. 12.

After the above seismic data enhancement, which resulted in remarkable additional improvement in the signal-to-noise ratio, I loaded one more seismic dataset into the Hampson-Russell AVO software, namely the P-wave velocity field obtained from the 3D reflection velocity analysis (see Table 3). This was necessary for the conversion of the source-receiver offsets to incident angles because AVO basically works in the incident angle domain, as it can be seen in Fig. 15.

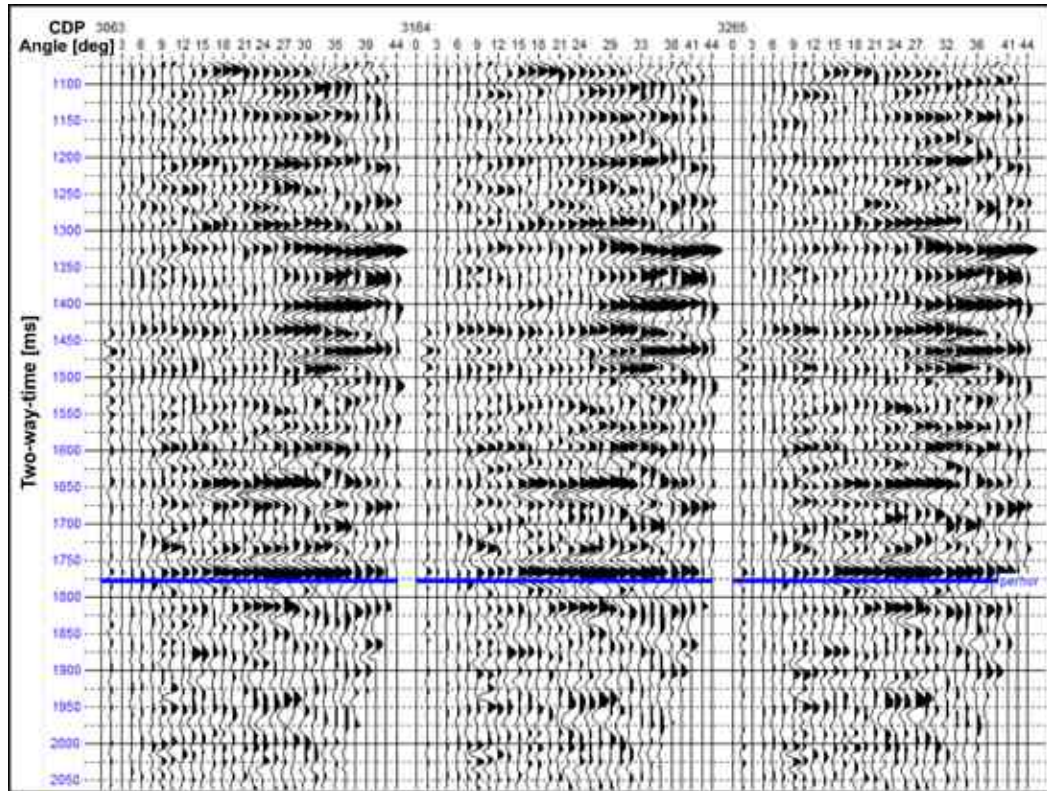


**Fig. 15** Angle gathers (0–44°) calculated from the CDP super gathers presented in Fig. 14. The blue horizon is explained in the caption of Fig. 12.

### 4.3. Seismic well tie

Well log data is measured in depth domain and its conversion into seismic two-way-time (TWT) will not give a good fit with the seismic traces of the time section for the first try. The reason is that depth to time conversion of any well log is performed by the acoustic logs ( $V_P$ ) and the velocity calculated from them differs from the seismic velocity. One of the reasons for that difference is the different frequency range of the acoustic logging (around 10,000–30,000 Hz) and the surface seismic observations (around 10–100 Hz). On the other hand, the drilling weakens the rocks, therefore acoustic logging provides lower velocity compared with the seismic velocity. On the third hand, acoustic logs usually start below the topographic surface (focused on a target zone) thus they do not provide velocity information for the upper part of the geological model. The missing velocity information is estimated by an upward extrapolation of the measured acoustic data (up to the surface), and this estimation can never be precise enough.

Because of the above reasons, a proper seismic well tie is necessary to get reliable time converted well logs to insert them into any surface seismic section. The procedure means shifting, stretching, and squeezing of the logs based on the similarity between the synthetic seismic traces obtained from the P-wave acoustic impedance ( $Z_P$ ) calculated from the P-wave velocity ( $V_P$ ) and the density ( $\rho$ ) logs at the location of the well.

I carried out an accurate seismic well tie in my study area utilizing the acoustic log ( $V_P$ ) measured in a productive well. The correlation coefficient between the synthetic and real seismic traces resulted in a value of 0.807, which can be considered as a remarkable high value. The correlation coefficient was obtained by a built-in process of the Hampson-Russell software calculating cross-correlation between the time series of the synthetic and real seismic traces. The closer the cross-correlation value is to 1.0, the more closely the compared traces are identical. Fig. 16 shows a great similarity between the seismic synthetic (blue) and the real (black) traces.

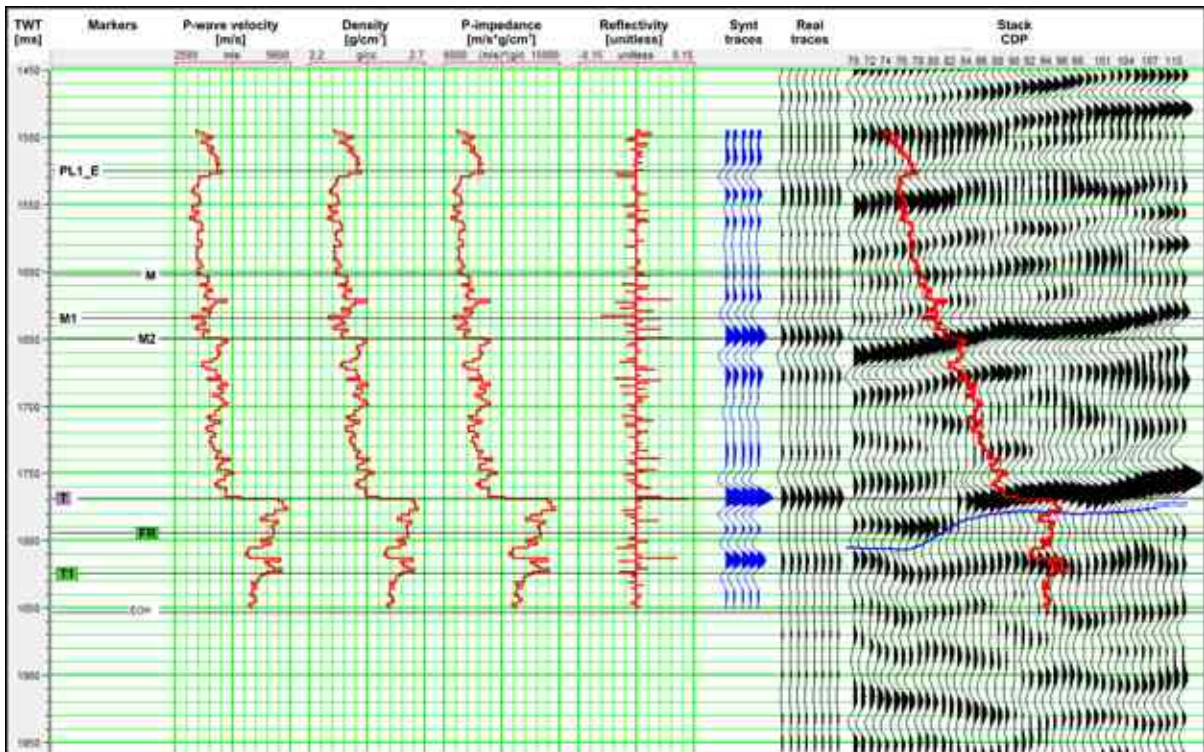


**Fig. 16** Results of the seismic well tie (modified after Masri and Takács 2022a). Tracks and panels from left to right are presented in time domain: P-wave velocity, density, acoustic impedance, reflectivity (red), synthetic seismic traces (blue), observed seismic traces (black), and the surface seismic data with the inserted P-wave acoustic impedance log. The blue horizon is explained in the caption of Fig. 12.

In Figs. 17 and 18, P-wave acoustic impedance log ( $Z_P$ ) before and after the seismic well tie is inserted in the closest seismic crossline chosen from the 3D data cube. The effect of the seismic well tie can be clearly seen in the figures. Before seismic well tie, the log doesn't fit to the seismic data at all but after the procedure it shows a nice fit to the seismic section. The procedure was performed manually, utilizing the interactive panels of the Hampson-Russell AVO software, looking for the best similarity between the synthetic and the measured seismic traces. Visual comparison and monitoring the correlation coefficient between the synthetic and real seismic traces supported finding the best fit.

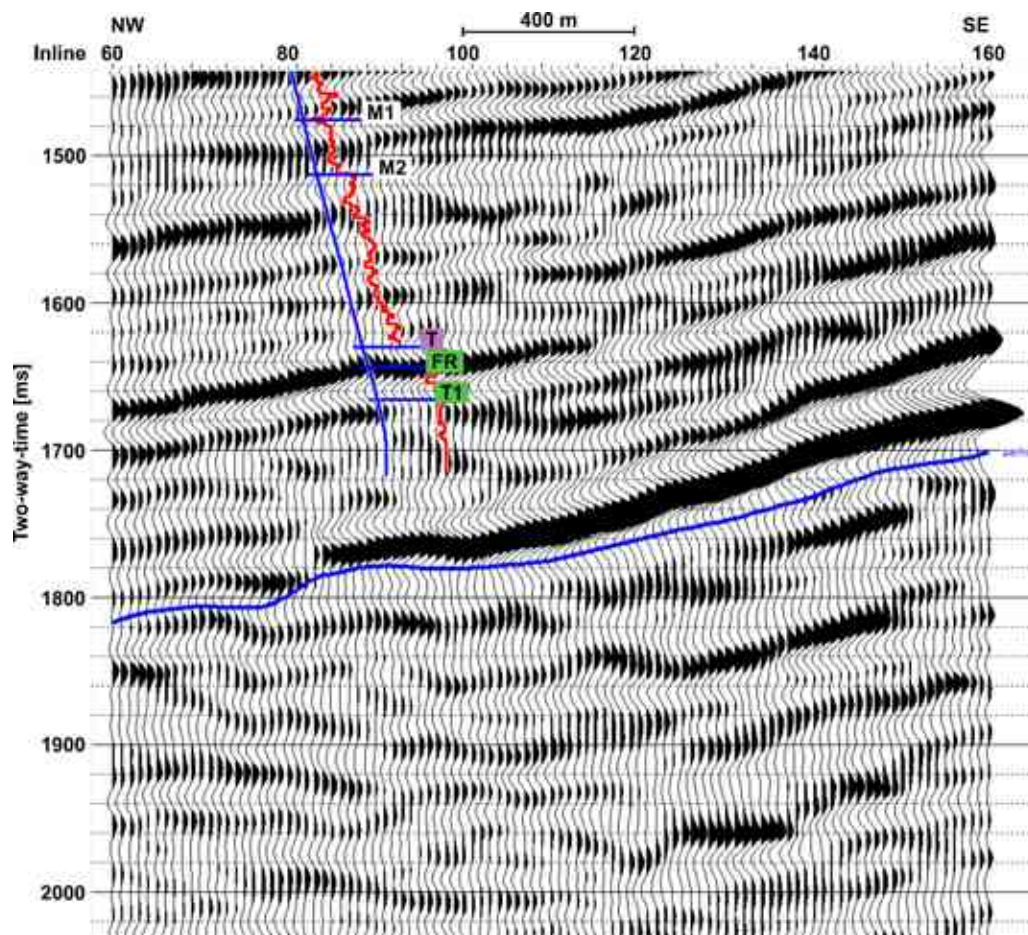


**Fig. 17** Raw P-wave acoustic impedance log before seismic well tie inserted in the seismic section (modified after Masri and Takács 2022a). Blue trace: well path, blue markers: tops of the geological formations, red log: acoustic impedance. The blue horizon marks a preliminary estimated top of reservoir marked at negative amplitudes assuming negative reflection coefficients.

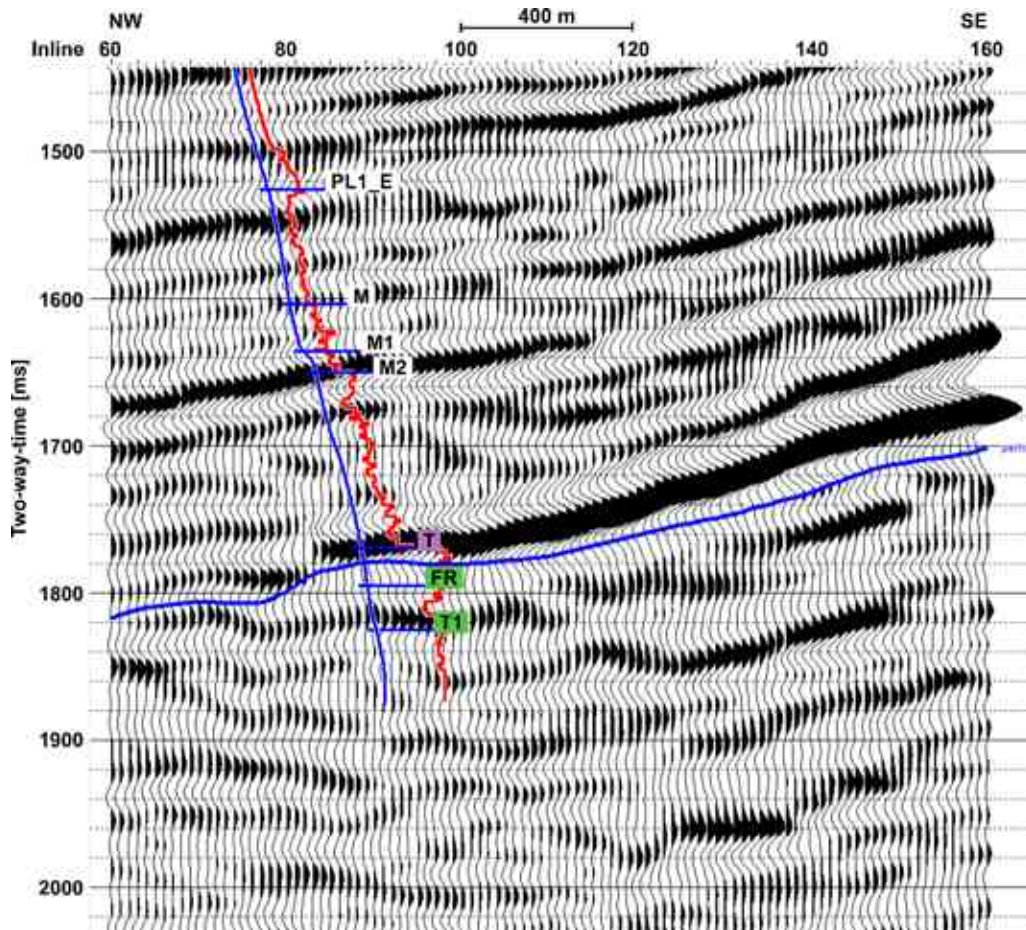


**Fig. 18** Correlated P-wave acoustic impedance log after seismic well tie inserted in the seismic section (modified after Masri and Takács 2022a). Blue trace: well path, blue markers: tops of the geological formations, red log: acoustic impedance. The blue horizon marks a preliminary estimated top of reservoir marked at negative amplitudes assuming negative reflection coefficients.

➤ **Thesis 2** on the seismic well tie:

I obtained excellent correlation coefficient (0.807) between the synthetic and observed seismic traces by an accurate seismic well tie, even though the well logging (i.e. the acoustic log) intersected variable geological formations in the Pliocene, Miocene, and Triassic sequences. I concluded that there are at least three different reasons for the initial misfit between the time-converted (uncorrelated) well logs and the observed seismic data. The causes are the different frequency range used for the acoustic logging and for the surface seismic observation, the weakened rocks caused by the drilling, and the missing velocity information between the surface and the starting point of the acoustic logs. A simple depth-to-time conversion of the well logs will result in poor correlation between the log data and the

surface seismic section. Precise seismic well tie (correlation) is a must before performing any seismic inversion procedure that utilizes the well log data.

## **5. INVERTED RESULTS AND DISCUSSION**

After the above preparation of the seismic and well log data (true amplitude data pre-processing and seismic well tie), I tested three inversion algorithms to study their results from the viewpoint of lithology discrimination and porosity indication. In the next chapters, they will be presented in the same historical order as they were introduced into the exploration. I will evaluate the results of the different inversion processes (post-stack acoustic impedance, pre-stack AVO, and pre-stack Simultaneous Model-based inversions), and I will compare the obtained rock physical attributes from the aspect of lithology discrimination and fluid detection inside the Triassic basement of my study area. I will show the P- and S-wave acoustic impedances, the density, as well as the Scaled Poisson's Ratio Change and the P- and S-wave velocity ratio attributes estimated from the same 3D seismic data and the available well logs. Finally, I will show the results of a subsequent Lambda-Mu-Rho transformation (related with the incompressibility and rigidity) along a vertical test profile. The base map of the available seismic and well logging data is presented in Fig. 19.

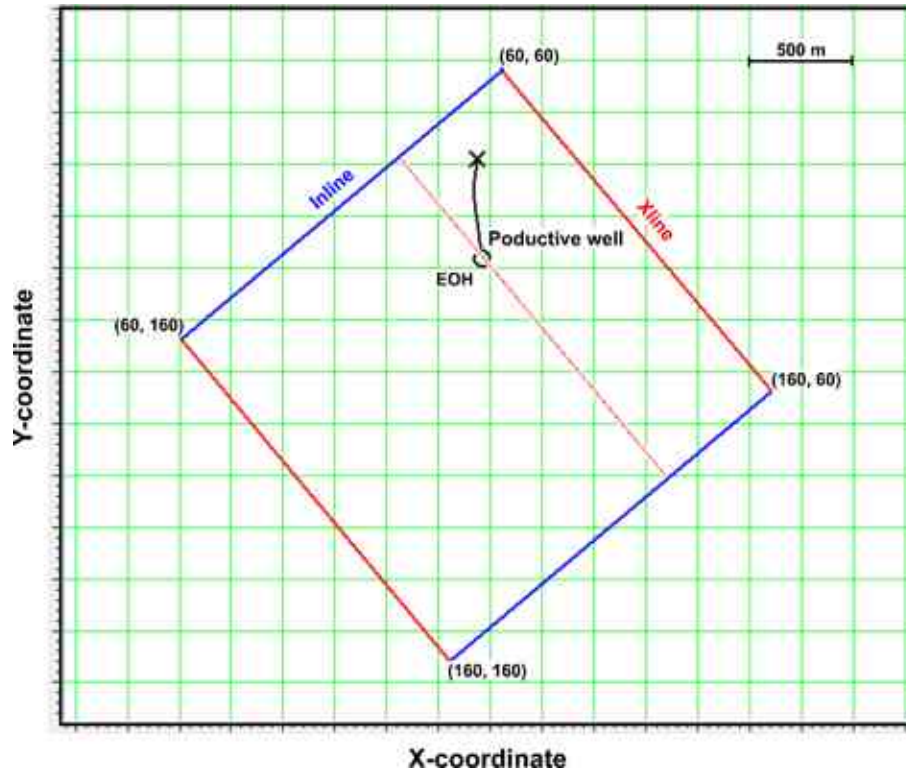


**Fig. 19** Basemap showing the limits of the true amplitude pre-processed 3D seismic data, as well as the locations of the deviated production well and the test profile (modified after Masri and Takács 2022b). EOH marks the end of sonic logging inside the Triassic basement. Coordinates are not presented for confidentiality reasons.

### 5.1. Traditional post-stack P-impedance inversion

The well-known traditional way to extend P-wave acoustic impedance data between and beyond the well log locations is the post-stack inversion of seismic data that are usually available in the surroundings of the boreholes. Lindseth (1979) assumed that the reflected amplitudes of a stacked seismic trace, on average, are proportional with the reflection coefficients. Based on this approximation,  $Z(t)$  relative acoustic impedance variations can be calculated by the equation

$$Z(t) = Z_0 \exp\left(2 \int_0^t R(t) dt\right)$$

where  $Z_0$  is the near surface acoustic impedance and  $R(t)$  is the reflectivity series down to the bottom of the investigated geological model. In other words, P-wave acoustic impedance

variations can be estimated by integrating the deconvolved seismic trace, then exponentiation, and finally scaling by  $Z_0$  (Lloyd and Margrave 2011). This procedure is applied on the post-stack seismic traces providing first the ‘high frequency relative variations’ of the P-wave impedance.

The ‘low frequency component’ of the P-wave impedance is calculated based on the product of sonic and density log values after applying a low pass filtering on the well log data. Finally, the ‘absolute seismic (pseudo-acoustic) impedance’ traces are obtained by the sum of the high-frequency and low frequency variations, after scaling the result at the location of the well. This simple algorithm provides a single P-wave acoustic impedance ( $Z_P$ ) volume. The calculation is fast and gives an appropriate result if we do not need S-wave impedance ( $Z_S$ ) information and other useful rock physical parameters such as the density ( $\rho$ ), and the P- and S-wave wave velocity ratio ( $V_P/V_S$ ) for more detailed lithology and porosity investigations.

An important step of the above entire post-stack procedure was the inversion analysis (Hampson-Russell Software Services Ltd. 2007) at the location of the production well. Fig. 20 represents remarkable high correlation (0.996) between the synthetic traces calculated from the inverted P-impedance values obtained from the seismic data (red curve) and the real seismic traces (black traces). The error (0.086) between them is negligible as it can be seen on the blue error traces.

Another helpful verification for the quality of inversion is the error between the real impedance log (drawn with blue) and the inverted impedance log (drawn with red). In my case this average (RMS) difference of the two logs was given as  $593.51 \text{ m/s} \cdot \text{g/cm}^3$ .

I note that the results of a similar but more sophisticated pre-stack inversion procedure will also be demonstrated in Chapter 5.3. That algorithm will provide several other helpful rock physical attributes in the study area.

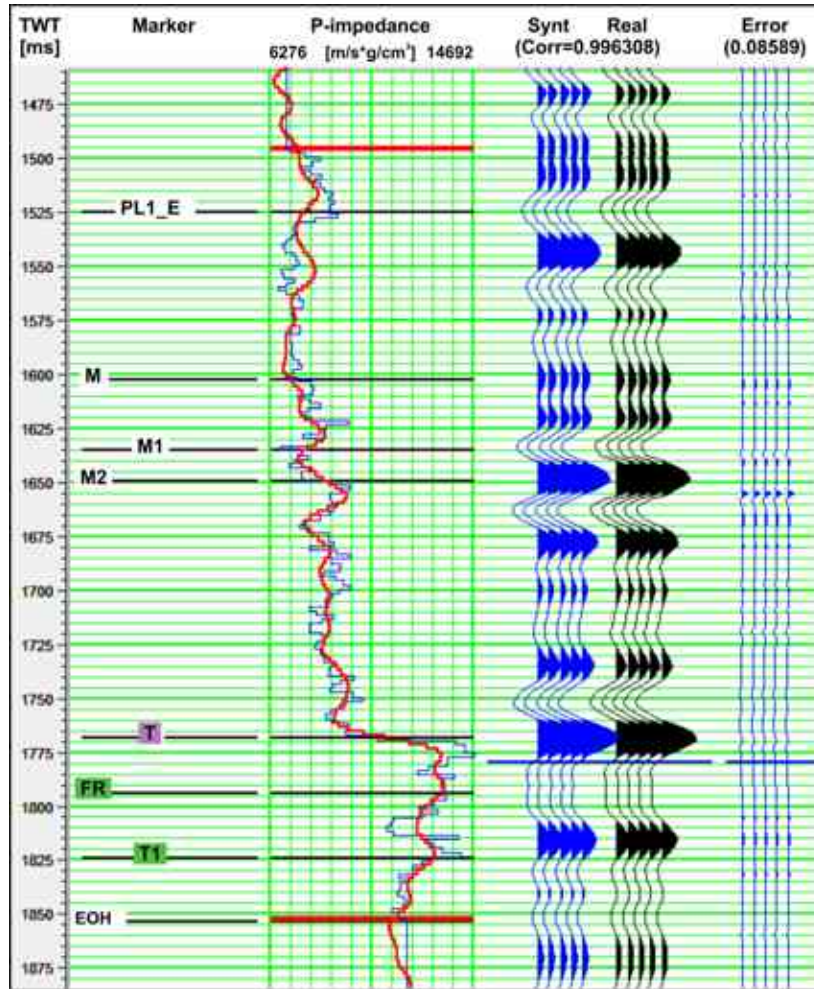


**Fig. 20** Original (blue) and inverted (red) P-impedance logs at the location of the well, as well as the synthetic seismic traces (blue) calculated from the inverted data; and the real (black) and error (blue) traces. The vertical axis is in two-way-time domain. The blue horizon in the seismic traces marks the estimated top of reservoir based on the conventional stack data. EOH means the end of logging.

In Fig. 21, the result of the above discussed traditional post-stack P-wave impedance inversion is shown. Notice the low P-impedance zone with light blue color between the top (FR) and the base (T1) of the Triassic fracture zone at the location of the production well. Similar low P-impedance features are usually characteristic for porous rocks (Chopra and Castagna 2014).

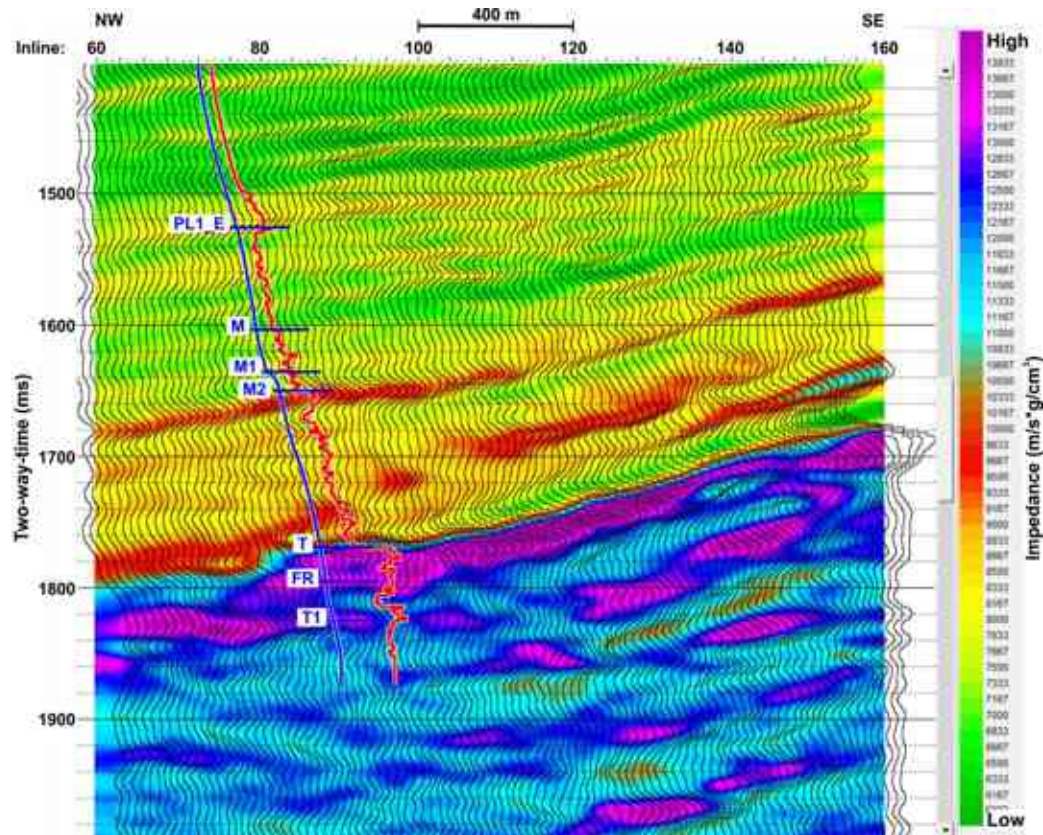


**Fig. 21** Inverted seismic P-wave impedance ( $Z_P$ ) section calculated from post-stack amplitude data, and inserted P-wave impedance log at the location of the well where FR marks the top of the fractured zone and T1 marks its base based on the drilling reports (Masri and Takács 2023). The magenta colors denote the highest acoustic impedance, and the green one denotes the lowest values.

➤ **Thesis 3** on the post-stack P-impedance inversion:

I applied traditional post-stack P-impedance ( $Z_P$ ) inversion on the true amplitude pre-processed 3D seismic and correlated well log data and concluded that this relatively simple inversion procedure provided surprisingly appropriate P-impedance model to detect a hot water bearing fractured dolomite zone of the Triassic basement of my study area. The top and the base of the fracture zone were known from well logging, and the inverted seismic model resulted in anomalously low P-impedance values at the location of the fractured interval revealed by a production well. However, the obtained rock physical model was not very helpful to discriminate the horizontally very variable lithology in the carbonate basement (fractured dolomite, friable dolomite, and Triassic marl). For this reason, I decided to perform subsequent pre-stack AVO and Simultaneous Model-based inversions to investigate the basement in detail.

## 5.2. Pre-stack AVO inversion

Mathematical backgrounds and calculation of the two basic AVO attributes (A–Intercept and B–Gradient), as well as their rock physical meanings were defined in Chapter 2.4, where I presented how to get those attributes from the pre-stack amplitudes of properly pre-processed CDP gathers (Fig. 5). The basic AVO attributes (A and B) are rarely applied alone because other very useful parameters, with more lithological meanings, can be derived from them. Currently, I believe that Scaled Poisson’s Ratio Change is one of the most helpful AVO indicators to detect fluid saturated porous geological formations by the pre-stack seismic data. Hilterman’s (1990) approach for the calculation is based on Shuey’s approximation (Eq. 1). Hilterman pointed out that if we assume the background Poisson’s ratio ( $\sigma$ ) equal to 1/3, then A+B is proportional to the change in Poisson’s ratio ( $\Delta\sigma$ ):

$$A + B = \frac{9}{4} \Delta\sigma.$$

In other words, the Scaled Poisson’s Ratio Change attribute can be derived from the basic AVO attributes in an easy way (in the range of incident angles 0–30°):

$$\text{Scaled Poisson’s Ratio Change} = \text{Intercept (A)} + \text{Gradient (B)}. \quad (2)$$

The above defined AVO attribute cross-section selected from the 3D data cube along the test profile is presented in Fig. 22.

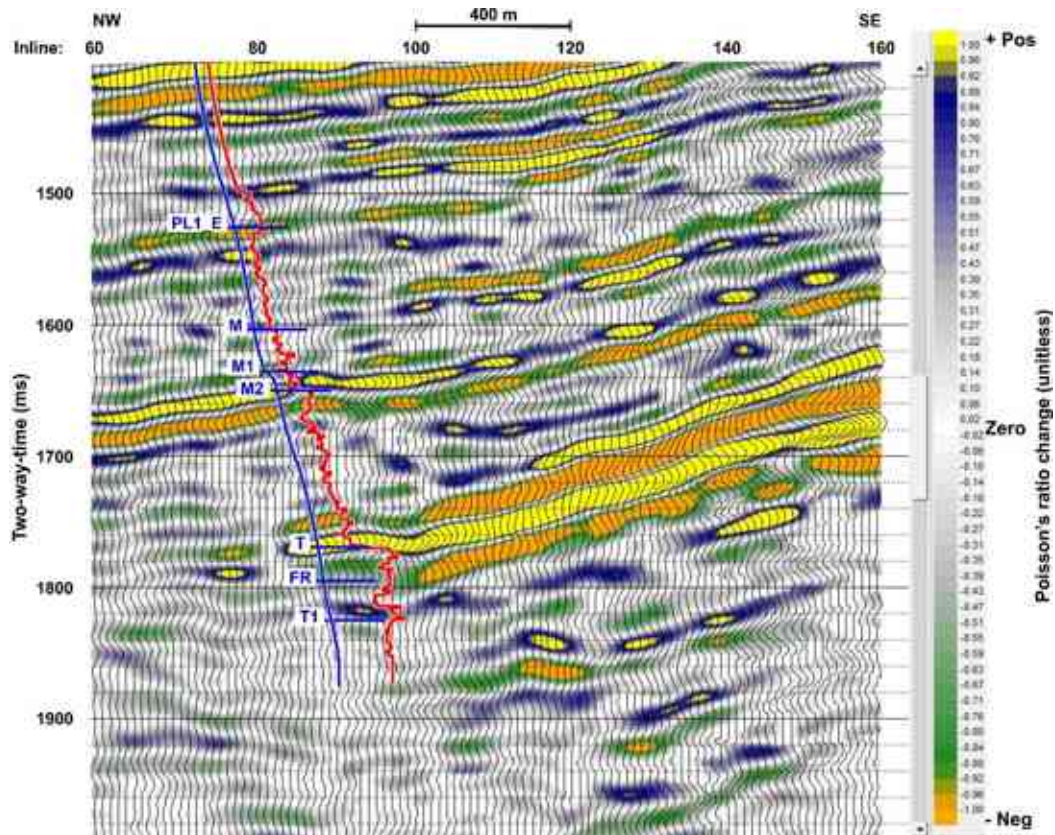


**Fig. 22** Acoustic impedance log after seismic well tie inserted in the Scaled Poisson's Ratio Change AVO attribute cross-section (modified after Masri and Takács 2022a). Blue trace: well path, blue markers: tops of geological formations, red log: acoustic impedance at the location of the well.

The most important conclusion, based on the above figure, is that Poisson's ratio is decreasing at the top of the fractured zone (marked with FR), and it is increasing at the base of the reservoir (marked with T1) revealed by the production well earlier. The green colors at around FR mean negative change in the Poisson's ratio while the blue colors at around T1 show positive change. This feature of the Poisson's ratio distribution is characteristic for the fluid saturated geological formations (Chopra and Castagna 2014), and the decreased values of the red P-wave impedance log between FR and T1 also indicate the fluid bearing dolomite zone very well. In addition, horizontal lithology variations in the Triassic basement become much more visible in the Scaled Poisson's Ratio Change AVO attribute section than they were shown in the post-stack P-wave impedance section presented in Fig. 21.

As I mentioned in the introduction part, three pairs of production and injection wells were drilled on the area of investigation and all those holes were drilled before carrying out the post- and pre-stack inversion procedures discussed in this dissertation. The reason that I

involved only one well in my study was that sonic logging unfortunately only in one production well penetrated deep enough in the Triassic basement. It must be also noted that the hole was planned remarkably well utilizing only the 3D migrated volume and some of its seismic attributes (reflection strength and variance). Based on the novel Scaled Poisson's Ratio Change attribute (Fig. 22), two important conclusions can be drawn. On the one hand, the well hit the northwestern edge of the Triassic fractured zone and evidently that was the most disturbed zone providing the highest porosity and permeability. On the other hand, very likely, the well passed through another porous zone in the Miocene sediments just beneath the M2 marker at about 1670 ms (see the decreasing values both in the Poisson's ratio and the acoustic impedance at that location). Obviously, they were focusing on the deeper Triassic formations for a higher temperature geothermal reservoir.

In the next parts of my dissertation, will I continue the lithological and structural investigations to perform pre-stack Simultaneous Model-based inversion and Lambda-Mu-Rho (LMR) transformation with the utilization of the available 3D seismic data and well logs. Those sophisticated procedures will provide additional models to study more rock physical attributes (P- and S-wave acoustic impedances, density,  $V_P/V_S$  ratio, and Lamé parameters) to complete the present interpretation and to draw conclusions about these specific inversion tools of the Seismic Lithology.

➤ **Thesis 4** on the pre-stack AVO inversion:

I carried out pre-stack AVO inversion on the true amplitude pre-processed 3D seismic and correlated well log data. I concluded that Scaled Poisson's Ratio Change ( $\Delta\sigma$ ) is a very helpful AVO attribute for detecting high temperature water bearing carbonate formations even in the Triassic dolomite basement of my study area. The Scaled Poisson's Ratio Change AVO attribute indicated decreasing values at the top of the fractured carbonate zone and increasing values at the base of the zone. This feature is very characteristic for the fluid saturated zones located in any geological formations. On the other hand, this pre-stack rock physical attribute allowed to get more detailed insight in the horizontal lithology variations of the pre-Cenozoic basement of the area of investigation than the earlier calculated post-stack P-impedance inversion did.

### 5.3. Pre-stack Simultaneous Model-based inversion

A relatively new trend in the seismic exploration is based on the pre-stack Simultaneous Model-based inversion of the amplitudes of seismic CDP gathers providing both the P- and S-wave acoustic impedance volumes, as well as the estimated density data. This methodology is often called as simultaneous Model-based inversion and, in my opinion, it can be utilized not only for the hydrocarbon exploration, but it might be a useful tool for the geothermal investigations. I will compare the result of the earlier discussed post-stack inversion with the results of the subsequent pre-stack acoustic impedance inversion utilizing the same seismic volume and well logs. I will analyze the new attribute sections (and some of their derivatives) obtained by the pre-stack algorithm in detail. Finally, I will draw the conclusions from the viewpoint of lithological discrimination and porosity detection in case of the studied complex carbonate geothermal reservoir located in the pre-Cenozoic basement of the Little Hungarian Plain.

The significant difference between the traditional post-stack impedance inversion and the modern pre-stack algorithm is demonstrated as follows. The modern pre-stack procedure provides not only a single P-wave impedance ( $Z_P$ ) volume as the post-stack algorithm does; but also, an S-wave impedance ( $Z_S$ ) cube and other derived rock physical parameters such as the P- and S-wave velocities ( $V_P$  and  $V_S$ ) and the density ( $\rho$ ). After getting those characteristic lithology parameters, other very helpful indicators related to the Lamé parameters ( $\lambda$ —incompressibility and  $\mu$ —rigidity) can be estimated by another subsequent process called Lambda-Mu-Rho (LMR) transformation (Goodway 2001, Russell and Hampson 2006).

Smith and Gidlow (1987) described the technology that can be used for converting the pre-stack reflected amplitudes of the CDP gathers into rock properties that are very beneficial to estimate lithology and porosity. In practice, Amplitude Versus Offset (AVO) inversion utilizes several approximations to solve the complex Zoeppritz (1919) matrix equation in different ways (for example the Aki and Richard 1980, the Shuey 1985, or the Fatti et al. 1994 simplifications). I note that my prior AVO inversion (Chapter 5.2) was performed using the Aki and Richard (1980) approach.

In this part of my dissertation, Fatti et al.'s (1994) theory was utilized given as

$$R(\theta) = (1 + \tan^2\theta) \frac{\Delta Z_P}{2Z_P} - 8 \left(\frac{V_S}{V_P}\right)^2 \sin^2\theta \frac{\Delta Z_S}{2Z_S}$$

where  $R(\theta)$  is the reflection coefficient versus incident angle ( $\theta$ ),  $Z_P$  and  $Z_S$  marks the P- and S-wave acoustic impedances, and  $V_P$  and  $V_S$  are the wave propagation velocities. The background  $V_S/V_P$  ratio should be known previously; however, Ma (2002) resolved this issue by replacing  $V_S/V_P$  by  $Z_S/Z_P$ . Other solutions (Hampson et al. 2005, Russel et al. 2006, Hampson-Russell Software Services Ltd. 2007) also prefer the P-wave and S-wave impedances, and the density parameters to be obtained from the pre-stack seismic data against getting the change in Poisson's ratio parameter (Eq. 2).

Fig. 23 shows the workflow of the Simultaneous Model-based inversion procedure based on the true amplitude pre-processed seismic gathers and the available well log data to obtain P- and S-impedance, and density parameters along the entire 3D seismic dataset. As I mentioned earlier, one of the great advantages of this procedure is that it can be followed by a subsequent calculation to obtain even more characteristic lithology and porosity indicators related to the Lamé parameters (incompressibility and rigidity).

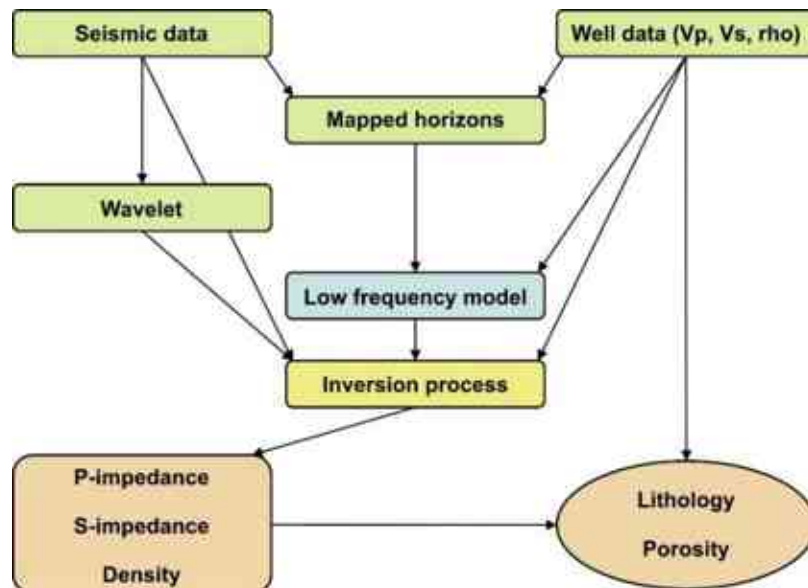


**Fig. 23** Simplified workflow of the Simultaneous Model-based pre-stack inversion procedure (Masri and Takács 2023)

The above inversion process is stabilized by the low frequency component of the available sonic and density log data obtained by low pass filtering (in my case 0-10 Hz). The low frequency information, conditioned by the lithology, is extended around and between the well locations using the interpreted horizons of the seismic sections (or volume). The resulted start model is often called as ‘low frequency’ or ‘course layer’ model. The ‘high frequency’ variations of the investigated rock physical parameters are calculated by the Simultaneous Model-based inversion of the pre-stack amplitudes of the CDP gathers. At the end, the final models are obtained with superimposing the high frequency variations to the low frequency models after scaling the results at the location of the well logs. This procedure allows to extend the well log data (sonic and density) based on the pre-stack seismic reflections and provides the rock physical parameters  $Z_P$ ,  $Z_S$ , and  $\rho$  in the surroundings of the well location (Hampson-Russell Software Services Ltd. 2007). Certainly, and naturally, the resolution of the resulted seismic models is lower than the resolution of the well logs involved in this procedure.

I will present the steps of the above workflow and the results obtained by the Simultaneous Model-based inversion. The inverted rock physical models will also be analyzed from the aspect of lithology and porosity mapping.

The first step of the procedure, similarly to any inversion algorithm, was the preparation of initial models for the inversion process. The initial  $V_P$  model was created by the spatial extrapolation of the low frequency (0-10 Hz) component of the measured sonic log utilizing a previously interpreted horizon, estimated as the top of reservoir, along the 3D seismic volume. Note that the same  $V_P$  start model was used for getting the result of the conventional post-stack inversion presented earlier. For the pre-stack process, the initial S-wave velocity ( $V_S$ ) and density ( $\rho$ ) data were calculated from the measured P-wave velocity data ( $V_P$ ) applying the Castagna et al. (1985) and Gardner et al. (1974) equations. The reason for those theoretical calculations was that measured Full Wave Sonic ( $V_S$ ) and density ( $\rho$ ) logs were not available in the study area. The lack of the measured  $V_S$  and  $\rho$  logs can affect a bit the accuracy of the inverted 3D rock physical models. However, the inversion was performed based on the measured pre-stack 3D seismic data (CDP gathers). The missing logs would have been used only for getting initial  $V_S$  and  $\rho$  models and for calibration of the final models at the location of the well. If the initial models and the calibration were not exactly precise that

would not affect the interpretation significantly. The reason is that mapping the hot water saturated zone(s) can be carried out based on the relative variations of the obtained rock physical parameters (decreasing or increasing). In this sense, the very precise absolute value of those models was not substantial. The low frequency initial P-wave acoustic impedance model ( $V_P \cdot \rho$ ) with the inserted P-wave impedance log is presented in Fig. 24.

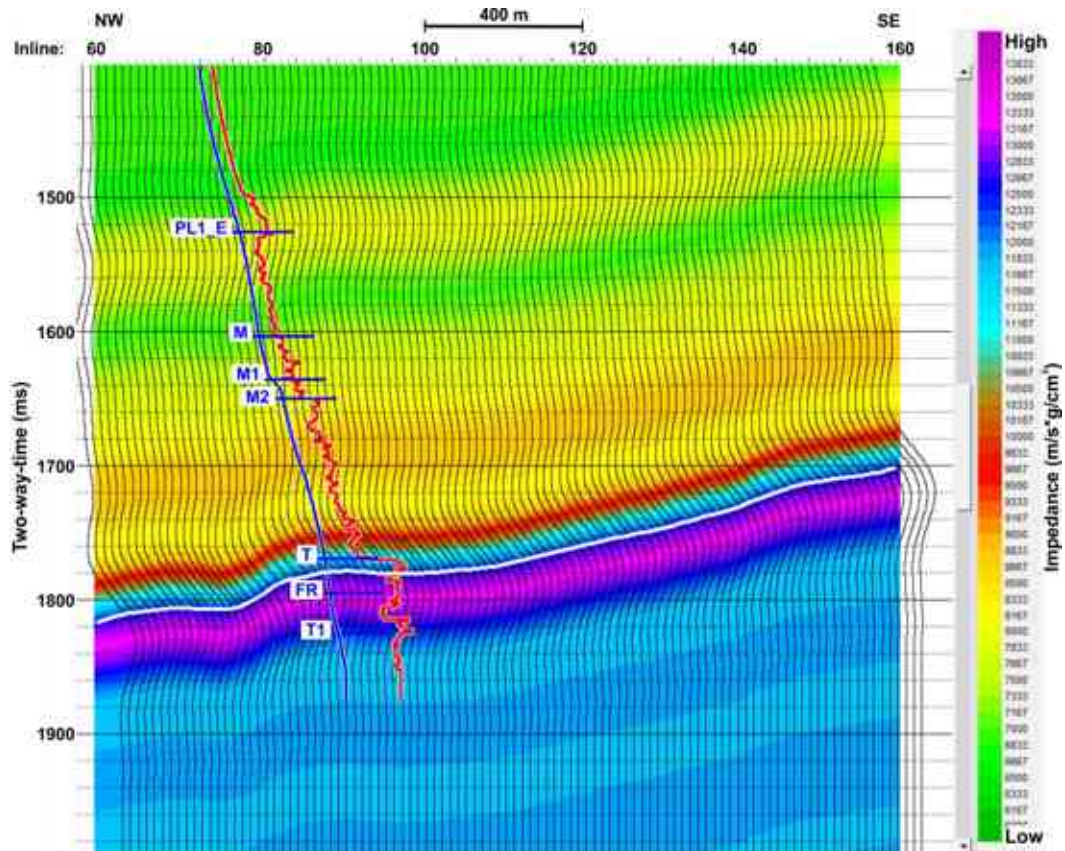


**Fig. 24** P-wave acoustic impedance ( $Z_P$ ) low frequency start model (0-10 Hz) built up based on extrapolated well log data (Masri and Takács 2023). The white horizon marks a previously interpreted seismic interface, according to the conventional seismic stack data, just beneath the top of the Triassic basement.

After setting up the low frequency initial models (0-10 Hz), high frequency variations (10-60 Hz) of the investigated  $Z_P$ ,  $Z_S$ , and  $\rho$  parameters were calculated by the simultaneous inversion of the reflected amplitudes based on the true amplitude processed CDP gathers. At the end, superposition of the initial models and the calculated relative changes provided the final results.

Before running the pre-stack Simultaneous Model-based inversion on the whole 3D seismic dataset, an inversion analysis at the location of the well was helpful to verify the inversion parameters and optimize the scaling of the seismic amplitudes based on the well logs. Two tests were involved in this preliminary inversion analysis. The first one included linear regression to determine background relation between the rock properties to stabilize the inversion process. Cross-plots of the available and calculated well log data provided the following background equations for the study area:

$$\ln(Z_S) = 1.42956 * \ln(Z_p) - 4.52683$$

$$\ln(\rho) = 0.2 * \ln(Z_p) - 0.93695$$

The second calculation of the inversion analysis performed at the well location was an estimation of a single scaler which was applied for the entire seismic dataset. This procedure sets up the RMS amplitude of the seismic traces equal to the RMS amplitude of the synthetic seismic traces calculated from the well log data. Fig. 25 shows the results: the measured and the inverted P- and S-wave impedance and the density logs; as well as the seismic synthetic, the real, and the error traces as a function of the incident angle. The wavelet to calculate the synthetic seismic traces was extracted from the real seismic traces, using statistical wavelet estimations for the near and far offsets, in the whole depth range of the well logging. The correlation coefficient between the synthetic and real data was 0.654, which value couldn't be regarded such a high correlation coefficient that was obtained from the post-stack seismic data (Chapter 5.1). However, the synthetic (red) and the real (black) traces show a very good similarity, and the error traces (red) didn't show any consistent flat events. Thus, we concluded that the inverted logs modeled the real data properly at the location of the well. I note that the depth range of the calculation window (1500-1850 m) included very variable lithology from the Lower Pannonian, Miocene, and Triassic formations. Perhaps this was the reason for not getting higher correlation in this case of the pre-stack inversion.

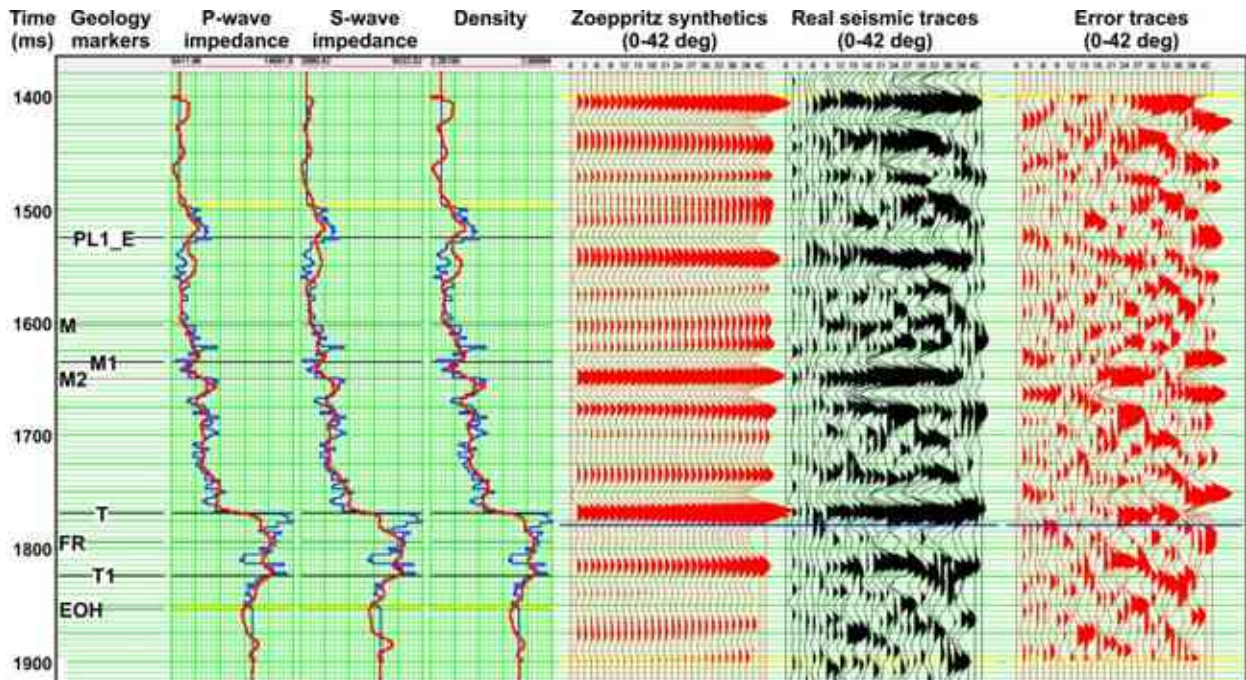


**Fig. 25** Original (blue) and inverted (red) P- and S-wave impedance and density logs at the location of the well, as well as the seismic synthetic (red), real (black) and error (red) traces (Masri and Takács 2023). The vertical axis is in two-way-time domain. The blue horizon in the seismic traces marks the estimated top of reservoir predicted based on the conventional stack data. EOH means the end of logging.

After the above local inversion analyses, the next step was the application of the Simultaneous Model-based inversion on the entire pre-stack 3D seismic dataset. Fig. 26 demonstrates the inverted pre-stack P-wave impedance model ( $Z_P$ ) along a vertical section located closest to the productive well. Based on the color scale, it shows decreased  $Z_P$  values inside the Triassic carbonates, between the top (FR) and the base (T1) of the known fractured zone. Note that low P-wave impedance value is one of the reliable indicators of the porous (fractured) rocks.

Let me take a short comment about the designation ‘Simultaneous Model-based inversion’ which is ambiguous because every inversion is model based. In my case, ‘model-based’ means that only the high frequency relative variations can be recovered from the reflected amplitudes. The absolute values of the rock physical model are obtained by the summation of the high frequency model and the low frequency component which comes from well logging data (sonic and density) after a low frequency filtering; as I discussed it in the Chapter 5.1.

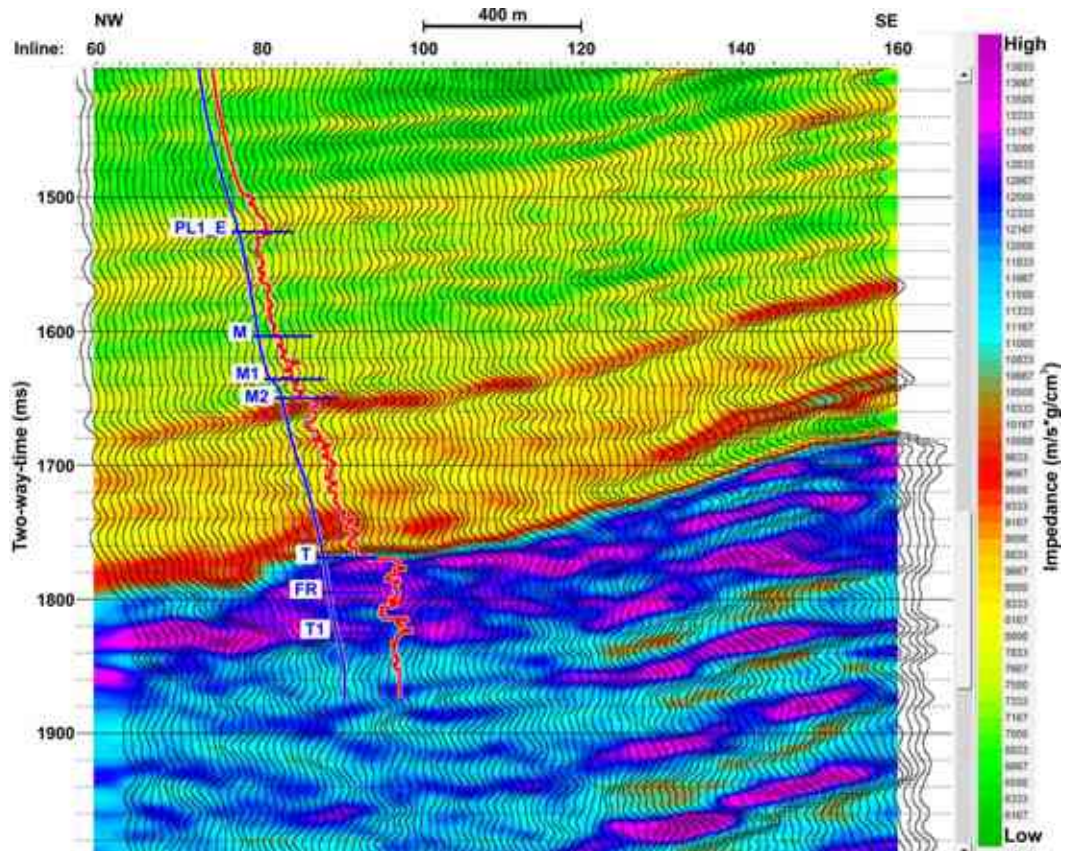
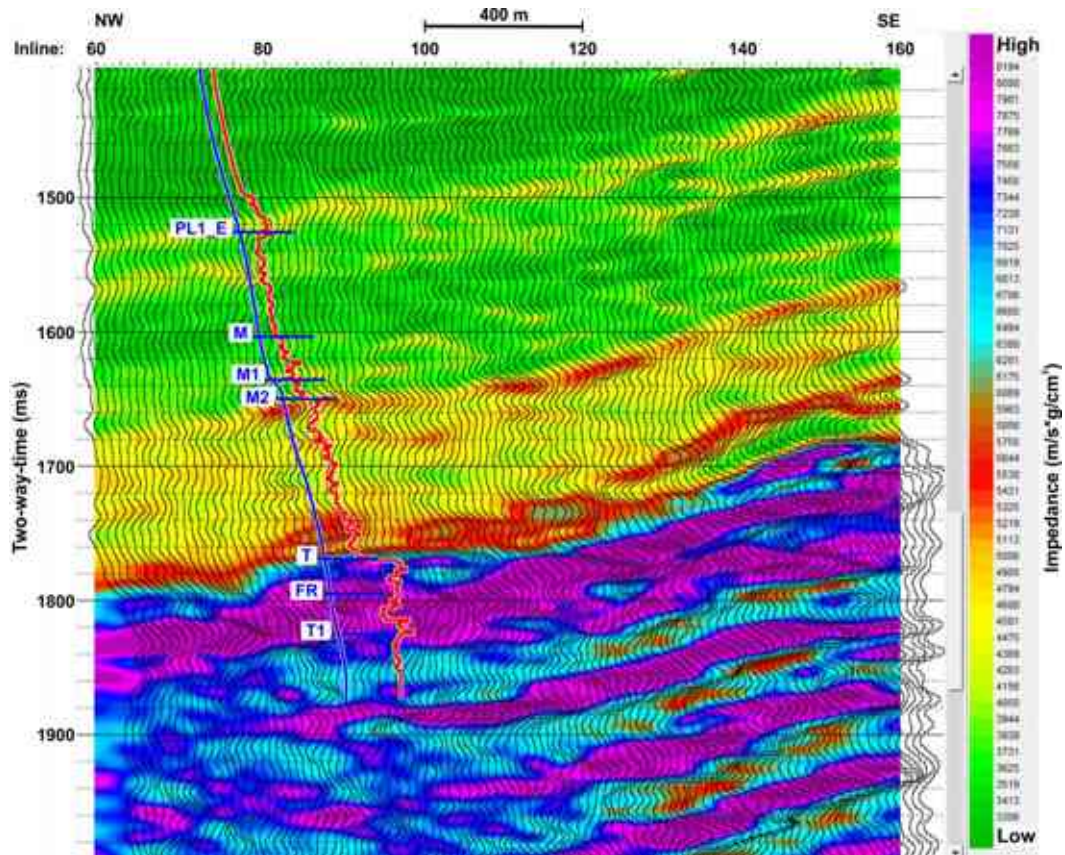


**Fig. 26** Inverted P-wave impedance ( $Z_P$ ) section calculated from the pre-stack seismic amplitude data and the available well logs (Masri and Takács 2023). P-wave acoustic impedance log is inserted in the section at the location of the well.

If we compare the above seismic attribute section ( $Z_P$ ) obtained from the pre-stack data with the result of the preliminary post-stack inversion (Fig. 21), we can clearly see that the pre-stack algorithm provided very similar but more detailed image than the post-stack inversion did. My recent finding agrees with Mallick's (2001) similar conclusion very well. However, neither of the post-stack or the pre-stack P-wave impedance calculations were good enough to distinguish the Triassic fracture zone (between the markers FR and T1) from the Triassic calcareous marl drilled beneath the T1 marker down to the end of hole (see Table 1). The reason could be that both the fractured dolomite and the calcareous marl can be characterized by low P-wave impedance values within the Triassic dolomite. Thus, we needed to create and study more rock physical attributes to solve this issue.

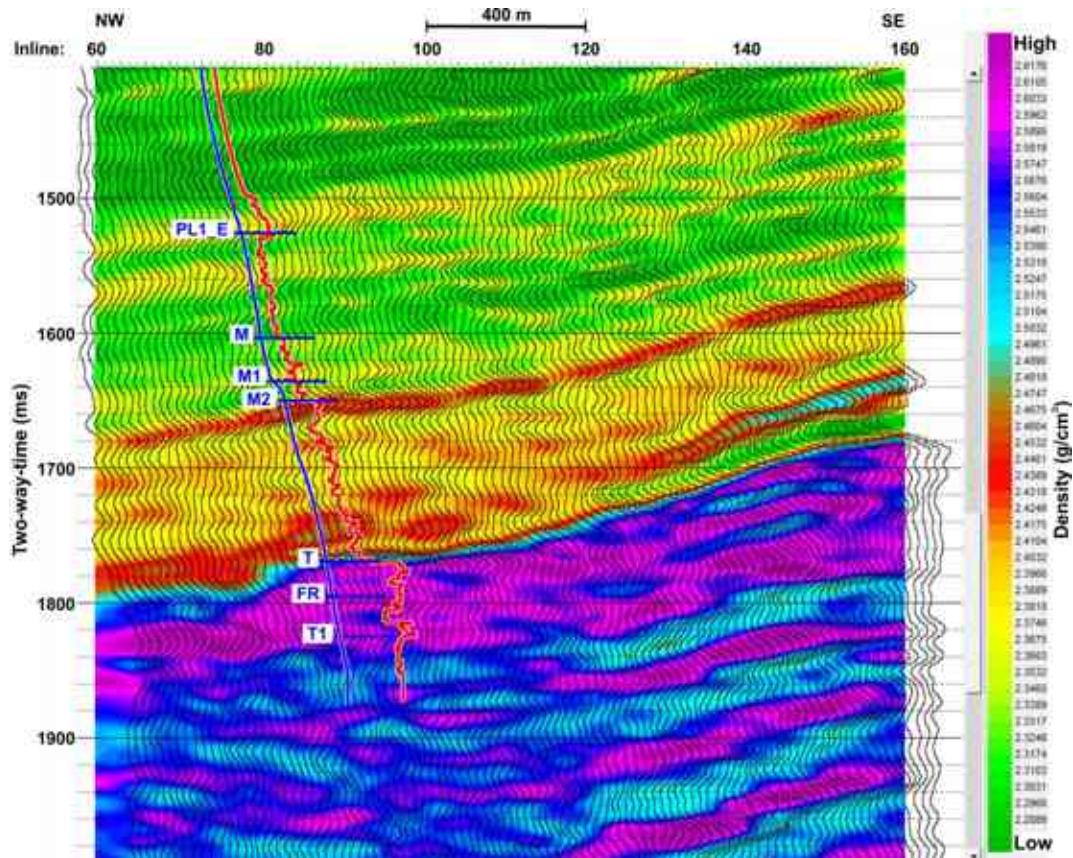
Fig. 27 shows the inverted S-wave impedance ( $Z_S$ ) section along the same test profile chosen very close to the well location. Looking at the inverted S-wave impedance data, it

doesn't show any changes in the interval of the fractured zone (FR–T1). The reason is that the S-wave doesn't see the pores or fractures because it cannot travel in fluids, it can travel only in the rock matrix.



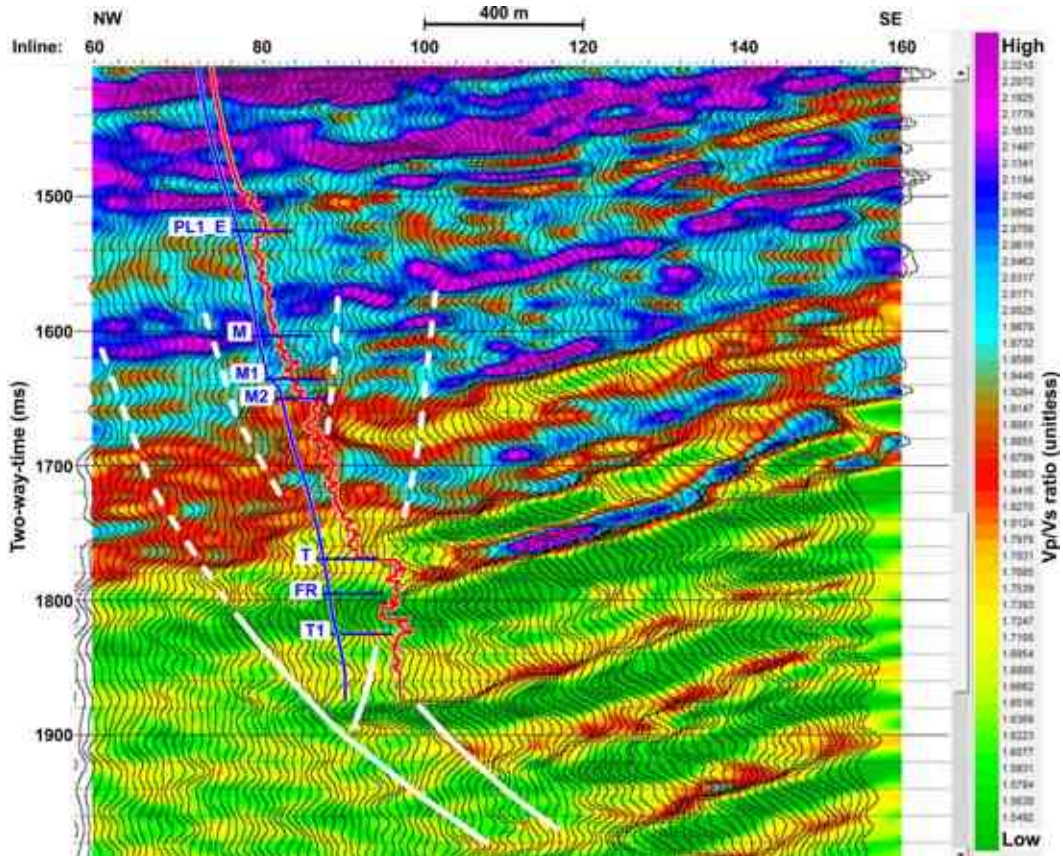
**Fig. 27** Inverted S-wave impedance ( $Z_s$ ) section calculated from the pre-stack seismic amplitude data and the available well logs (Masri and Takács 2023). P-wave acoustic impedance log is inserted in the section at the location of the well.

Fig. 28 presents the inverted density ( $\rho$ ) section showing just a very moderate decrease in the fractured dolomite zone (between FR and T1). At this moment, I am not sure why the inverted density data doesn't detect the fracture zone more characteristically. One possible reason could be that there was no density log measured in the well, it was synthesized from the measured sonic log (Gardner et al. 1974). The other and very likely reason is that extracting density information from the seismic observations is very difficult because of its low sensitivity to the reflected amplitudes.



**Fig. 28** Inverted density ( $\rho$ ) section calculated from the pre-stack seismic amplitude data and the available well logs (Masri and Takács 2023). P-wave acoustic impedance log is inserted in the section at the location of the well.

$V_P/V_S$  velocity ratio is demonstrated along the same profile in Fig. 29. This is the most detailed image that I got in this study by now. It shows a zone of very low  $V_P/V_S$  values at the porous zone (between the FR and T1 markers), namely the dark green zone just beneath the top of the reservoir (FR). Beneath the T1 marker, bit higher values appear with yellow colors down to the bottom of the hole. Based on this  $V_P/V_S$  attribute section, I believe that inside the Triassic basement, on the SE side of the well, the dark green colors indicate cyclic variations of hot water bearing dolomite zones; and the yellow and red ones indicate marl and dolomite without fracturing (or only with a very low porosity). In the NW side of the well, inside the Triassic basement, the lithology prediction is still not totally clear, but the seismic feature is evidently different (light green and yellow coded  $V_P/V_S$  values) from the other part of the profile.



**Fig. 29** Derived  $V_P/V_S$  velocity ratio section calculated from the pre-stack seismic amplitude data and the available well logs (Masri and Takács 2023). P-wave acoustic impedance log is inserted in the section at the location of the well.

The explanation for the above discussed lithology model, which fits very well to the drilling data (Table 1), is that the Poisson's ratio and consequently the  $V_P/V_S$  ratio for marl are usually higher than they are for fluid saturated dolomite zones as it will be shown in Fig. 30. Before that, it must be noted that the Poisson's ratio and the  $V_P/V_S$  ratio parameters are much more characteristic for the lithology and the porosity than the P-wave acoustic impedance ( $Z_P$ ). Poisson's ratio ( $\sigma$ ) is expressed by the following equation, where  $V_P$  and  $V_S$  are the P- and S-wave propagation velocities:

$$\sigma = (V_P^2 - 2V_S^2)/2(V_P^2 - V_S^2)$$

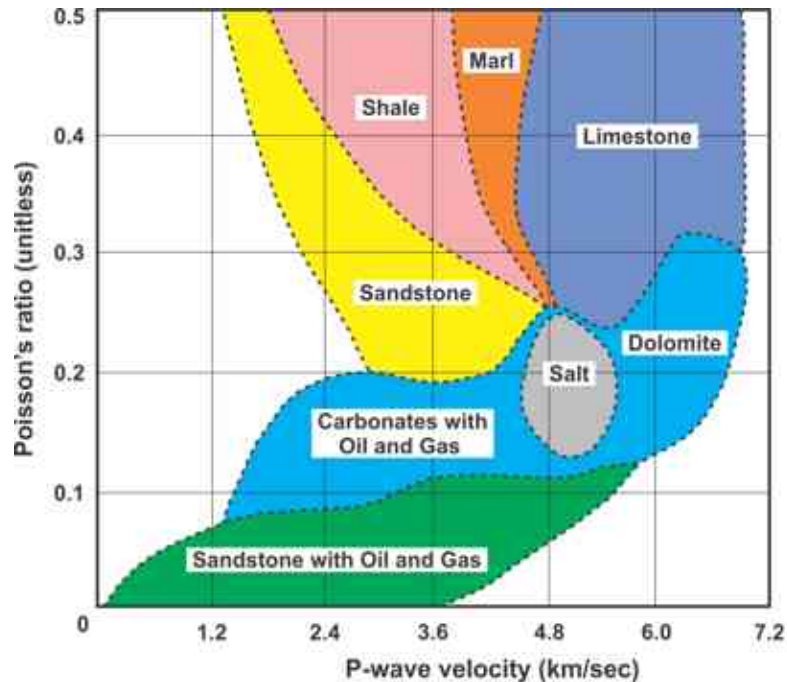


**Fig. 30** Poisson's ratio versus P-wave velocity parameters for different lithology (redrawn after Miles et al. 1989). Poisson's ratio is a nonlinear function of  $V_P/V_S$  and lower Poisson's ratio means lower  $V_P/V_S$  ratio. Color coding is independent from the colors of the seismic attribute sections.

The  $V_P/V_S$  ratio attribute section presented in Fig. 29 suggests significant spatial variations in the lithology of the Triassic basement. It is clearly seen, by the color scale, that the basement lithology is different at the two sides of the productive well. The reason for that can be the major fault zone, probably a strike slip, marked with white segments in the figure. On the left (NW) side of the fault zone, I got moderate  $V_P/V_S$  ratio changes appearing with light green and yellow colors – very likely indicating Triassic friable dolomite and marl. On the right (SE) side of the fault zone, the variations are much more significant (dark green, yellow, and red colors) – very likely detecting a cyclic series of high porosity dolomite, clayey dolomite with very low porosity, and perhaps marl. In my opinion, this complex vertical fabric of the reservoir was developed by the variation of the sea level. Based on this image, I believe that the location of the productive well (drilled years before this study) was planned very carefully by focusing on the structural elements of the prior, conventional 3D migrated stack volume. My recent study revealed a much more detailed lithology model. Based on that, I can say that they drilled the northwestern edge of a complex geothermal reservoir located in the Triassic basement at a highly permeable structural zone. The former, accurate well planning

resulted in the very successful productive well with the water temperature bit higher than 100 °C supplied at the surface.

To accept or reject the lithology model discussed above, a subsequent Lambda-Mu-Rho (LMR) transformation will provide other helpful elastic parameters related to the Lamé parameters (incompressibility and rigidity). That procedure will offer more useful rock physical information to verify the above model.

➤ **Thesis 5** on the pre-stack Simultaneous Model-based inversion:

The pre-stack Simultaneous Model-based inversion provided several additional rock physical attributes for my investigation on the study area. I concluded that the pre-stack P-wave impedance ( $Z_P$ ) data proved to be more detailed than the post-stack one produced beforehand. It indicated the Triassic fracture zone very well; however, it still didn't allow distinguishing the fractured dolomite, friable dolomite, and marl inside the basement. On the other hand, the S-wave impedance ( $Z_S$ ) attribute could not be helpful to indicate the fractured zone at all because S-wave does not propagate in porous media. Neither the obtained density ( $\rho$ ) attribute turned to be a good porosity indicator, likely because deriving density information from seismic data is a very difficult task. However, I derived the P- and S-wave velocity ratio ( $V_P/V_S$ ) from the above rock physical attributes and pointed out that it was a very good indicator to separate the Triassic fracture zone from the Triassic marl.

#### **5.4. Additional Lambda-Mu-Rho transformation**

To verify or possibly modify my lithology and porosity findings discussed in the previous chapters, the so-called Lambda-Mu-Rho (LMR) transformation was used to estimate even more elasticity parameters (Goodway 2001, Chopra and Castagna 2014). The procedure provided additional useful information for the verification of the above models.

The first and second Lamé parameters ( $\lambda$ -incompressibility and  $\mu$ -rigidity), like the earlier discussed Scaled Poisson's Ratio Change ( $\Delta\sigma$ ) and  $V_P/V_S$  ratio, are similarly characteristic rock physics properties and can be expressed by the following relationships:

$$\begin{aligned}\lambda &= \rho(V_P^2 - 2V_S^2) \\ \mu &= \rho V_S^2\end{aligned}\tag{3}$$

where  $\rho$  is the rock density and  $V_P$  and  $V_S$  are the velocities of the two wave types in the rock. The software used for the Simultaneous Model-based inversion (Hampson-Russell Software Services Ltd. 2007), as mentioned above, produces P- and S-wave impedance and density data. After the pre-stack inversion has been performed, it gives the possibility to carry out a subsequent LMR transformation to obtain the Elastic Impedances ( $\text{Lambda} \cdot \text{Rho} - \lambda\rho$  and  $\text{Mu} \cdot \text{Rho} - \mu\rho$ ).

In the next part of this chapter, I will examine the above elastic parameters, but first I want to present a preliminary interpretation on the two most helpful rock physical attributes found until now (Scaled Poisson's Ratio Change and VP/VS ratio). I was focusing on the upper part of the Triassic basement (Figs. 31 and 32), and the interpretation is based on the relative variations of those estimated rock physical parameters keeping in view the diagram demonstrated in Fig. 30.

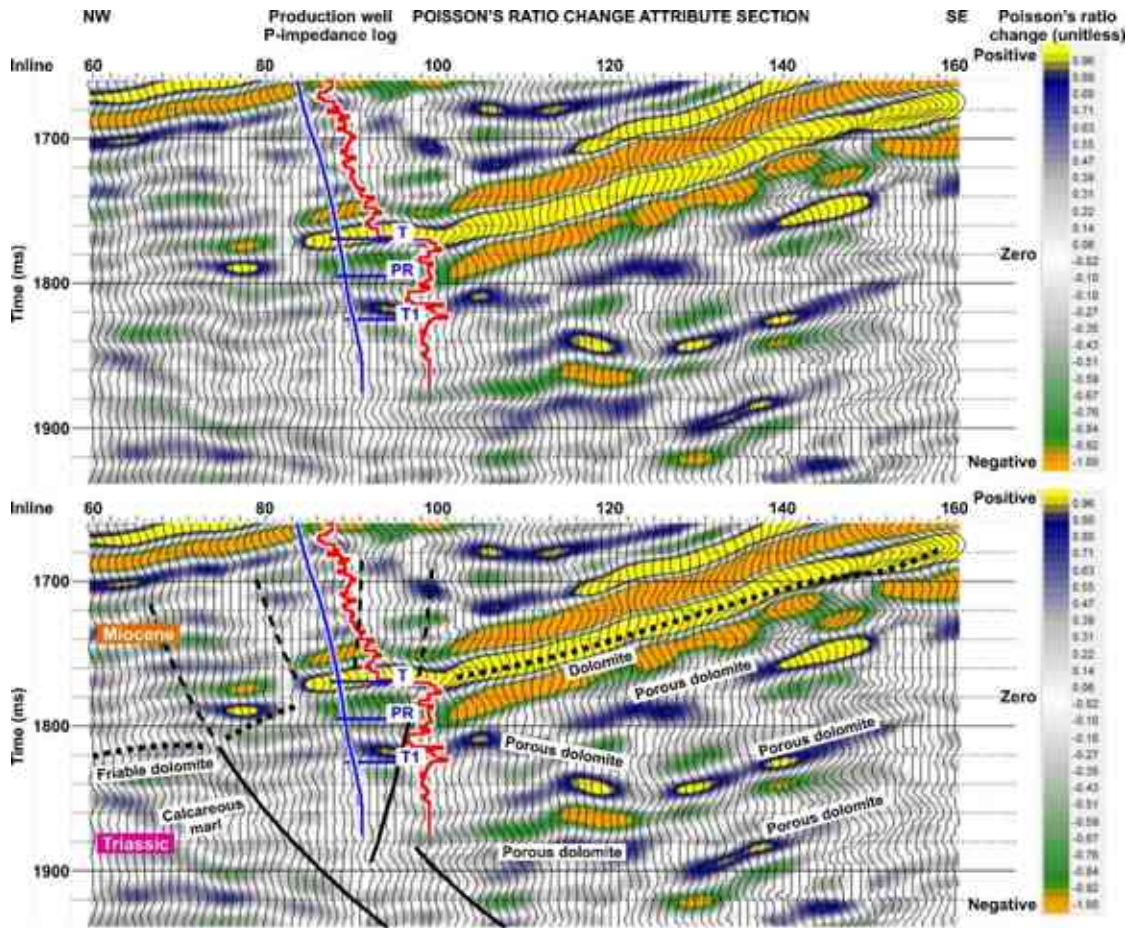


**Fig. 31** Scaled Poisson's Ratio Change ( $\Delta\sigma$ ) attribute plot and lithological interpretation with P-wave impedance log inserted at the location of the production well. Markers PR and T1 indicate the top and bottom of the fractured zone determined in the borehole.

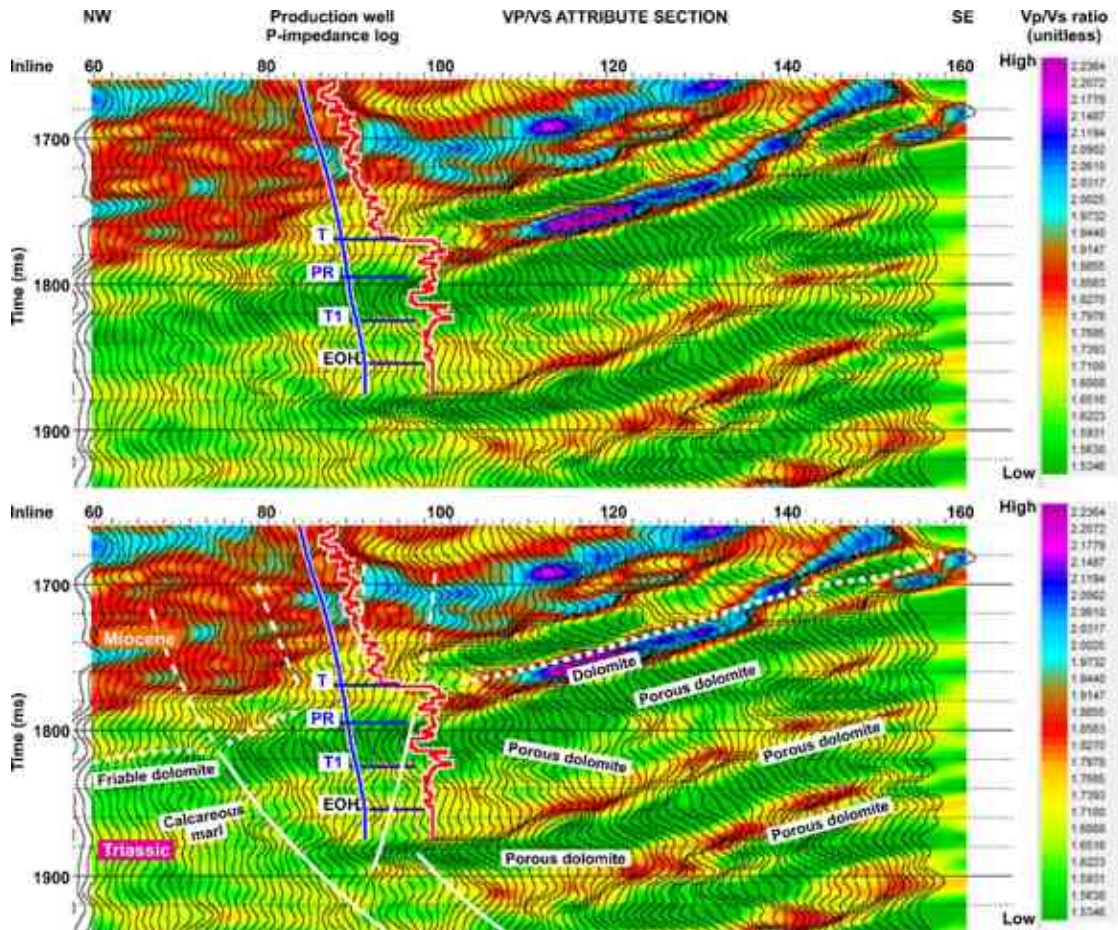


**Fig. 32**  $V_P/V_S$  velocity ratio attribute plot and lithological interpretation with P-wave impedance log inserted at the location of the production well. Markers PR and T1 indicate the top and bottom of the fractured zone determined in the borehole.

New attribute sections resulted by the LMR transformation are presented in Figs. 33 and 34. It is important to note that the lithological interpretation labelled in the figures were transferred from the Scaled Poisson's Ratio Change and  $V_P/V_S$  ratio sections to the  $\Lambda \cdot \rho$  and  $\mu \cdot \rho$  sections based on that primary interpretation. To make the present interpretation more precise on the lithology and porosity, the diagram shown in Fig. 35 (Goodway 2001) can provide helpful information. However, it can be clearly seen that the  $\Lambda \cdot \rho$  ( $\lambda\rho$ ) attribute shows the horizontal lithology variations inside the Triassic basement much better than the  $\mu \cdot \rho$  ( $\mu\rho$ ) attribute does. In other words,  $\mu \cdot \rho$  is not too sensitive for the porosity because it is related with the S-wave propagation velocity and the density of the rocks (Eq. 3) and S-wave cannot propagate in the pore space of the rocks, as I mentioned earlier (Chapter 2.2).

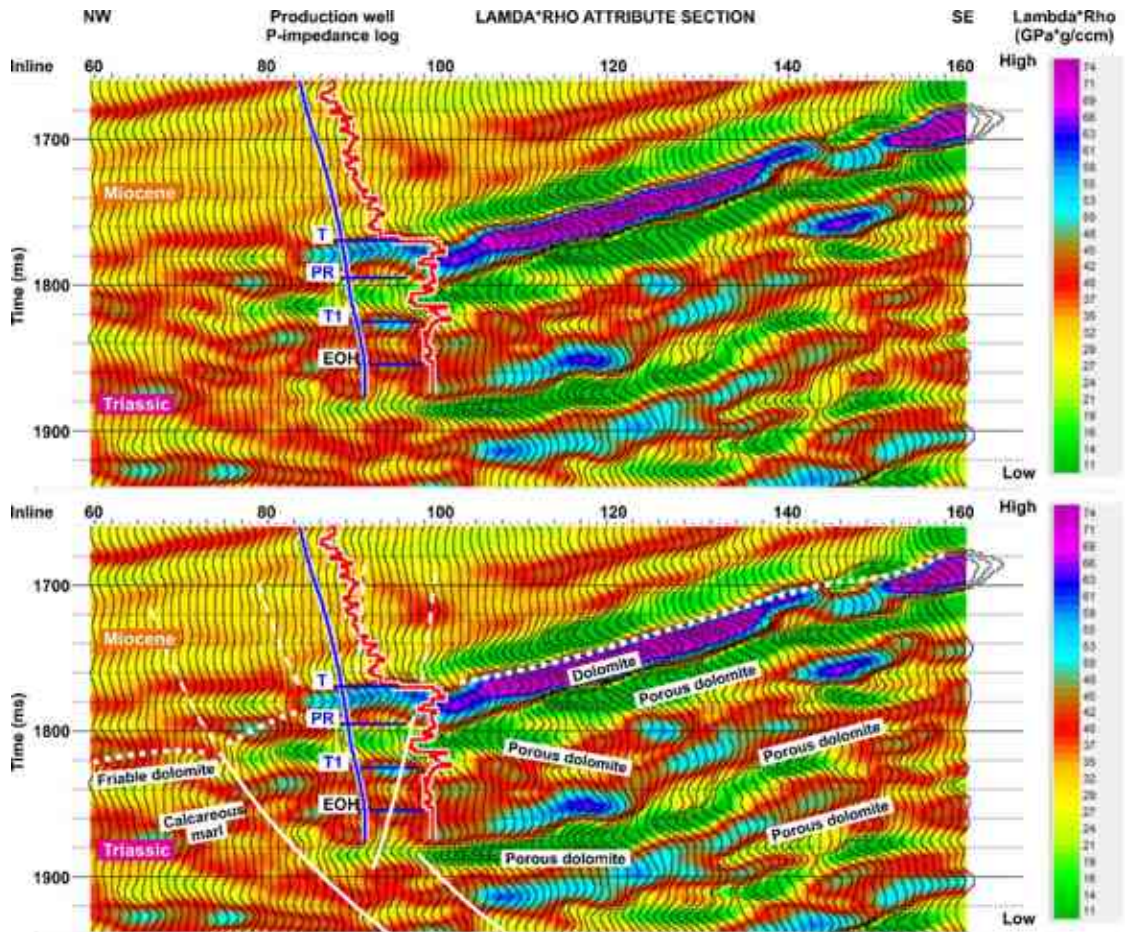


**Fig. 33** Lambda\*Rho ( $\lambda\rho$ ) attribute plot and lithological interpretation with P-wave impedance log inserted at the location of the production well. Markers PR and T1 indicate the top and bottom of the fractured zone determined in the borehole.

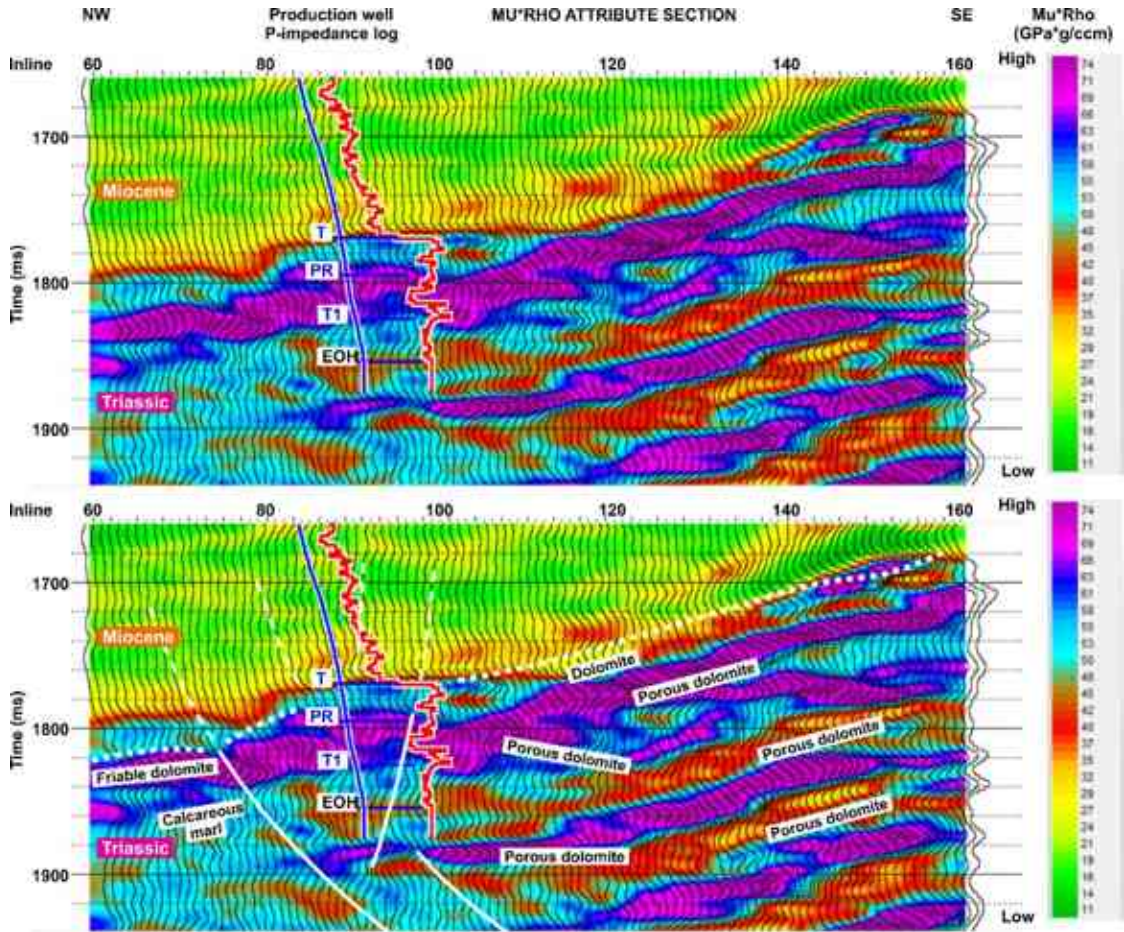


**Fig. 34**  $\mu\rho$  attribute plot and lithological interpretation with P-wave impedance log inserted at the location of the production well. Markers PR and T1 indicate the top and bottom of the fractured zone determined in the borehole.

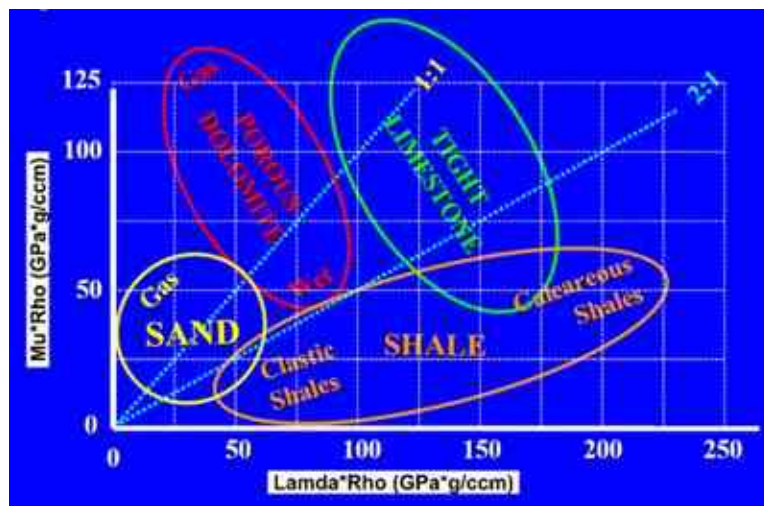


**Fig. 35**  $\mu\rho$  versus  $\lambda\rho$  parameters for different lithology (after Goodway 2001). Color coding is independent from the colors of the seismic attribute sections.

➤ **Thesis 6** on the Lambda-Mu-Rho (LMR) transformation:

I analyzed several rock physical attributes (P- and S-wave impedances, density, Scaled Poisson's Ratio Change,  $V_P/V_S$  ratio, as well as the Lambda\*Rho and Mu\*Rho parameters) obtained by three different inversion algorithms and a subsequent LMR transformation applied on the same, properly pre-processed 3D seismic data and well logs. I compared all results of the conventional post-stack P-impedance inversion, the modern pre-stack AVO inversion, and the novel pre-stack Simultaneous Model-based inversion utilizing the available seismic and well log datasets. I was focusing on a known geothermal reservoir located inside the Triassic basement and concluded that three of the calculated rock physical parameters, namely the Scaled Poisson's Ratio Change, the  $V_P/V_S$  ratio, and the Lambda\*Rho attributes provided the best results for porosity indication and lithology discrimination inside the very complex carbonate basement of my study area.

## **6. TRACKING THE FRACTURE ZONE**

The ultimate task of any geological-geophysical exploration is to assign prospective drilling locations to hit the hydrocarbon or geothermal reservoir (or in other cases the mineralization zone). Drilling is expensive, especially inside the pre-Cenozoic basement of the Pannonian Basin. In the next parts of my study, I will demonstrate how to reduce the risk of drilling by the properly prepared and interpreted rock physical attributes obtained by seismic inversion algorithms.

### **6.1. Cross-plotting the fracture zone(s)**

Cross-plotting the inverted rock physical parameters was a useful tool to visualize the Triassic fracture zone(s) along the same vertical seismic profile that has been presented in the earlier parts of my dissertation. This tool enables the interpreter to perform a quantitative analysis on the rock physical parameters obtained by the utilization of inversion procedures carried out on the seismic data. The benefit of the analysis is that we can display and interpret any cross-plot of two available rock physical parameters and select a range of them that we want to display along any vertical profile of the 3D seismic cube (Hampson-Russell Software

Services Ltd. 2007). In this way, the lithological formations having the selected rock physical parameters can be visualized in any vertical sections of the 3D seismic data cube.

I was focusing mainly on the fractured dolomite zones containing fluid and I chose to study two different combinations of the inverted rock physical parameters:

- P- and S-wave velocity ratio ( $V_P/V_S$ ) versus P-impedance ( $Z_P$ ), and
- $\mu \cdot \rho$  ( $\mu\rho$ ) versus  $\lambda \cdot \rho$  ( $\lambda\rho$ ).

The above parameters have turned to be out as prominent porosity indicators inside the Triassic basement of my study area. The ranges of the investigated rock physical parameters for three types of lithology (fractured dolomite, calcareous marl, and dolomite); and the results of cross-plotting along the cross section can be seen in Figs. 36 and 37. The colors of the presented section highlight the reflections coming from the studied lithological formations (green – fractured dolomite, orange – calcareous marl, blue – dolomite). All results of the analyses confirmed my former assumption, concluded based on the individual rock physical models, that the earlier presented production well was drilled at the northwestern edge of a complex geothermal reservoir.

Note that cross-plotting was carried out only for the Triassic basement but for the whole 3D seismic data cube utilizing 1,275,675 data points. The resulted lithology sections presented below show good fit to the drilling data at the location of the production well. The highlighted fracture zone (green) fits excellently to the drillhole between the markers FR and T1. The calcareous marl feature (orange) obtained from the seismic data also meets very well to the drilling data between the T1 and EOH (end of logging) markers. At the same time, there is some ambiguity at the top of the basement (T) where a mix of clay marl, friable dolomite, and dolomite was described in the drilling report (see Table 1). However, dolomite (blue) does appear right at the FR marker. I would say that the demonstrated cross-plotting and its results provided a good ‘skeleton’ for the lithology discrimination. AVO responses of open and clay filled fractures in the magmatic basement of the Athabasca Basin, Keefe Lake area, North Canada had been discussed by Takács et al. (2015) for the purpose of uranium exploration.

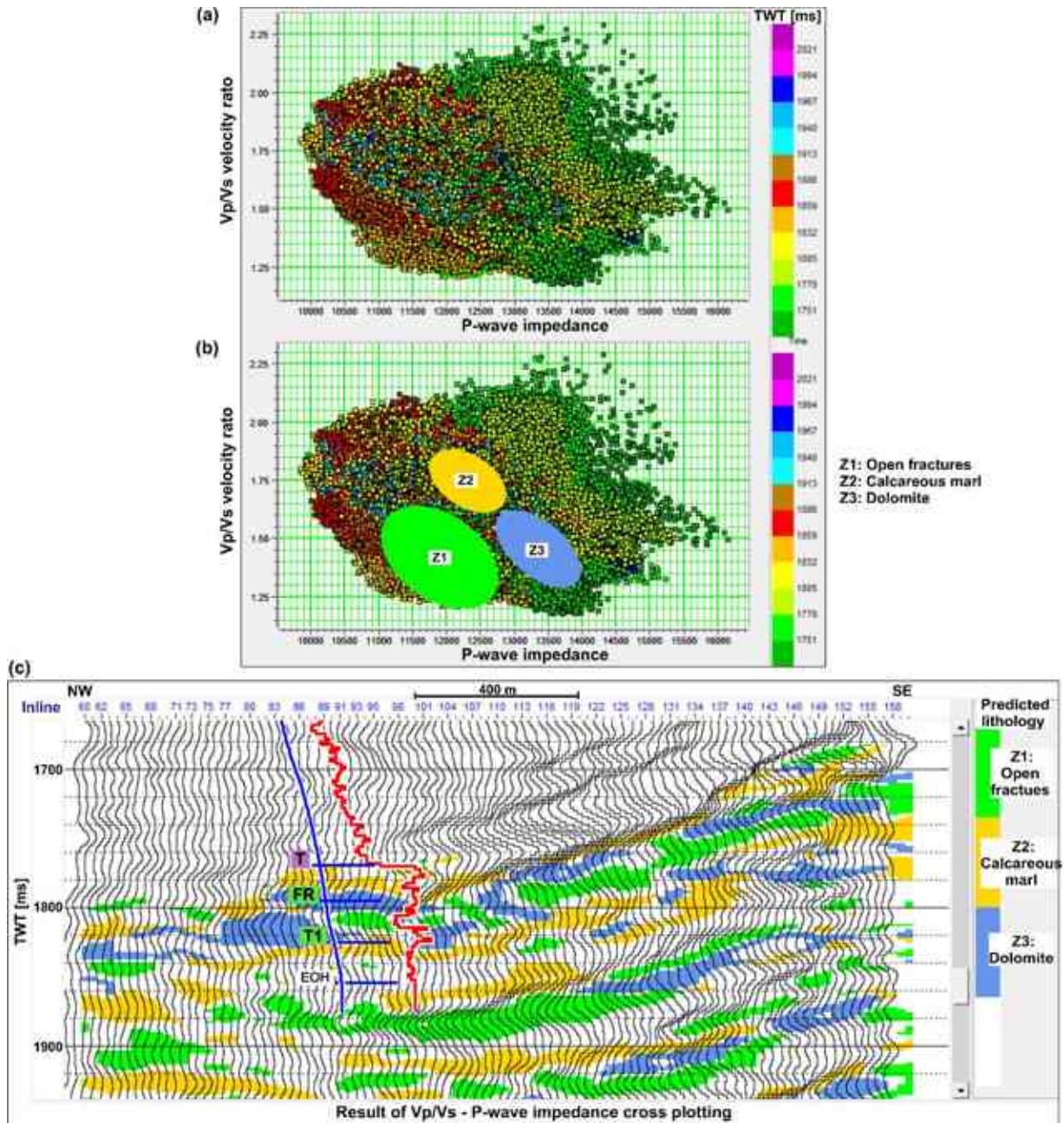


**Fig. 36** P- and S-wave velocity ratio ( $V_p/V_s$ ) versus P-impedance ( $Z_p$ ) cross-plots of the inverted seismic data (a and b) and the highlighted zones along the test profile (c). It should be noted that the cross-plot samples are colored by TWT [ms] while the section is coded by lithology: green – open fractures, orange – calcareous marl, blue – dolomite. The length of the demonstrated lithological section is 2 km (see Fig. 19).

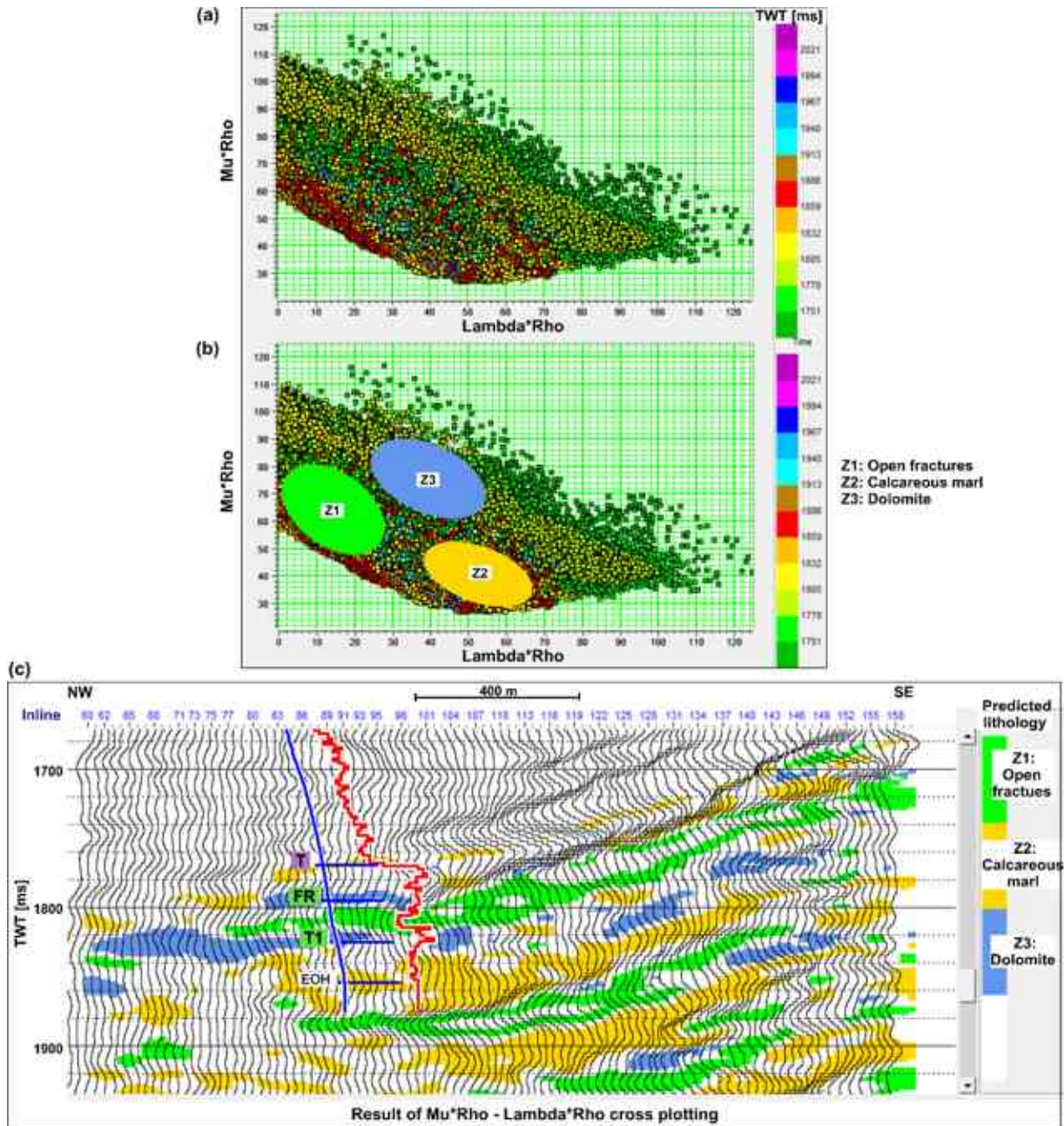


**Fig. 37**  $\text{Mu}^*\text{Rho}$  ( $\mu\rho$ ) versus  $\text{Lambda}^*\text{Rho}$  ( $\lambda\rho$ ) cross-plots of the inverted seismic data (a and b) and the highlighted zones along the test profile (c). It should be noted that the cross-plot samples are colored by TWT [ms] while the section is coded by lithology: green – open fractures, orange – calcareous marl, blue – dolomite. The length of the demonstrated lithological section is 2 km (see Fig. 19).

## 6.2. Spatial mapping of the inverted elastic parameters

After the above cross-plot analysis, I carried out spatial mapping to display three inverted rock physical parameters that had been proved to be very characteristic for the fracture zone:

- Scaled Poisson's Ratio Change ( $\Delta\sigma$ ),
- P- and S-wave velocity ratio ( $V_P/V_S$ ), and
- Lambda\*Rho ( $\lambda\rho$ ).

Spatial mapping was performed along the a priori interpreted surface of the estimated top of the Triassic reservoir, which was correlated based on the conventional migrated 3D stack volume. The resulted rock physical maps along that surface are presented in Figs. 38, 39, and 40.

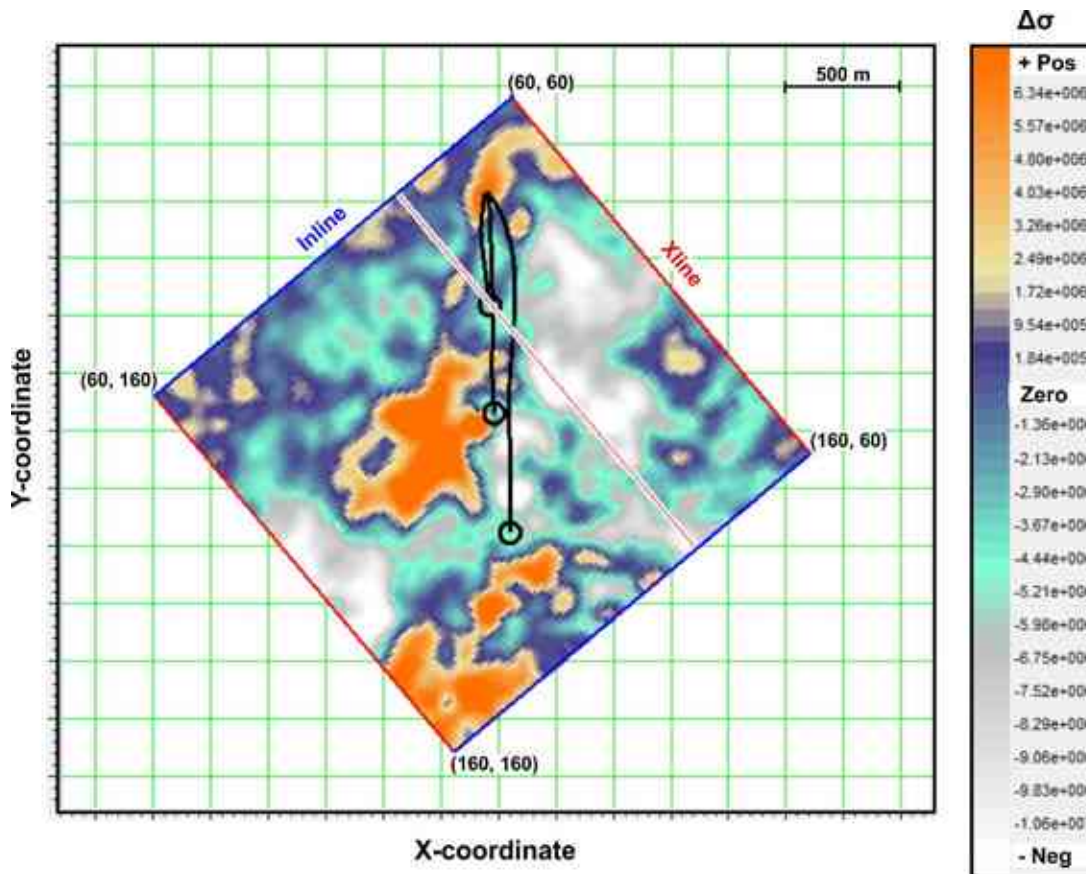


**Fig. 38** Scaled Poisson's Ratio Change ( $\Delta\sigma$ ) map along the a priori estimated top surface of the Triassic geothermal reservoir. Black trajectories mark the paths of three deviated production wells and black circles mark the bottom of the holes. The test cross-section is marked with a red line with white edge. Coordinates are not presented by confidentiality reasons.

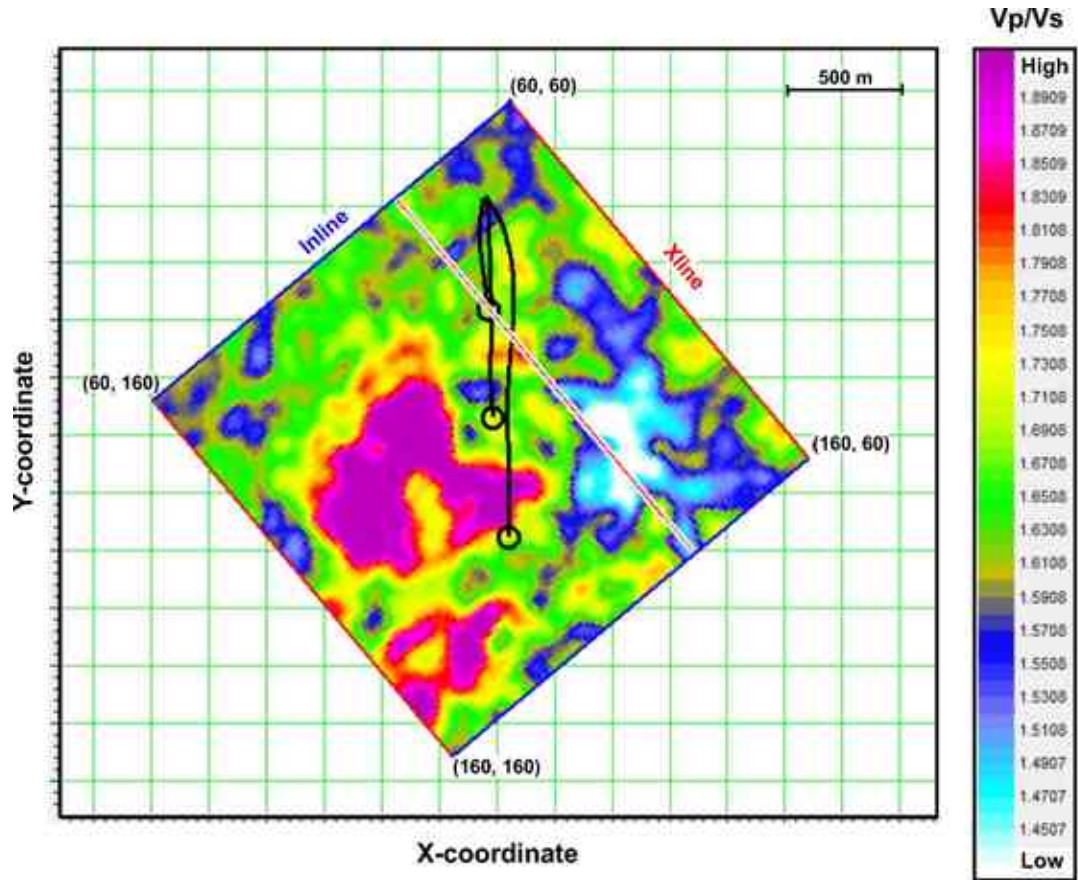
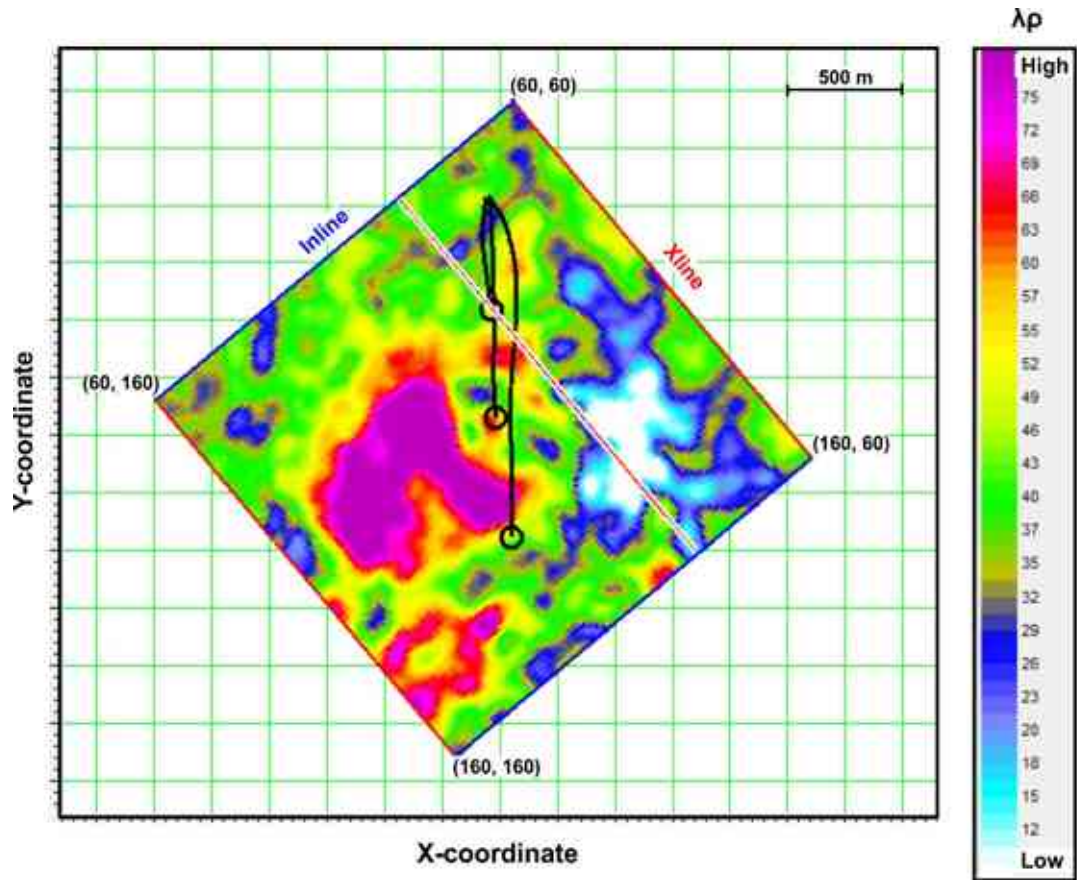


Fig. 39 P- and S-wave velocity ratio ( $V_p/V_s$ ) map along the a priori estimated top surface of the Triassic geothermal reservoir. See caption of Fig. 38 for more explanation.



**Fig. 40** Lambda\*Rho ( $\lambda\rho$ ) map along the a priori interpreted top of the investigated Triassic geothermal reservoir. See caption of Fig. 38 for more explanation.

It should be noted that altogether three production wells, marked in the above maps, hit the reservoir prior the recent Amplitude Versus Offset (AVO) and Simultaneous Model-based inversions, as well as the Lambda-Mu-Rho (LMR) transformation. The reason that I involved only one of them in my earlier calculations was that only one sonic log penetrated in the basement and intersected the uppermost fracture zone. Thus, only one hole provided useful rock physical information for the Triassic target zone.

The extension of the presented maps (2 x 2 km) is less than the available larger seismic dataset, because I had to reduce the running time of the time-consuming pre-stack migration process during the data preparation by cutting around the data. However, all maps show very well that the demonstrated rock properties are helpful for well planning because they revealed the weak zones of lithology fabric in the target zone of my study area. I believe that the demonstrated inversion procedures adopted from the hydrocarbon exploration can also be successful in the geothermal exploration to assign promising drilling targets.

The Scaled Poisson's Ratio Change map (Fig. 38) illustrates the values at the a priori estimated surface of the top of reservoir and this elastic parameter has both positive and negative values. The relatively large negative numbers (significant decreasing in Poisson's ratio at the studied surface) are indicators of the fluid content. In other words, white, grey, and light blue areas demonstrate promising locations for drilling. The P- and S-wave velocity ratio and the Lambda\*Rho maps (Figs. 39 and 40) represent median values in a time window (10 ms) just below the same surface. Those parameters have only positive values, and the low numbers (white, blue, and green) indicate the porous formations. Comparing the three maps, it can be seen that they show similar distribution of the investigated parameters; consequently, lithological conclusions can be drawn from them for well planning.

➤ **Thesis 7** on the cross-plotting and spatial mapping

I provided useful lithological information based on cross-plotting and spatial mapping of several rock physical parameters (Scaled Poisson's Ratio Change, P-impedance,  $V_P/V_S$  ratio, Lambda\*Rho, and Mu\*Rho). On the one hand, fractured dolomite, calcareous marl, and dolomite were successfully discriminated in vertical sections. On the other hand, I concluded that three production wells drilled before my recent analyses were planned very accurately based on the only available conventional migrated stacks at that time. Based on the novel inverted rock physical models, all production holes hit the western part of a complex Triassic reservoir in a fault zone; and the major volume of the reservoir system is in east direction from the wells. It has a cyclic structure which was supposedly evolved by the variation of the sea level. The methodology that I presented in my dissertation can help with well planning in future geothermal investigations.

## 7. SUMMARY

Focusing on a high temperature geothermal reservoir located in the Triassic basement of the Little Hungarian Plain, Hungary, I draw several conclusions that can be useful for further investigations in other study areas. I utilized properly pre-processed seismic and well log data for my study and demonstrated that a hot water bearing fracture zone in the dolomite basement can be successfully mapped by seismic and well logging inversions (pre-stack Amplitude Versus Offset and Simultaneous Model-based inversions, as well as a subsequent Lambda-Mu-Rho transformation). True amplitude seismic data pre-processing and seismic well tie were essential steps before the inversion processes. I summarize the most relevant results as follows.

By modelling theoretical AVO responses in my study area, I concluded that the AVO response of the investigated geothermal reservoir (located in the carbonate basement) is different from the usually increasing response of a gas bearing clastic sandstone. The amplitude versus incident angle variations from the investigated carbonate reservoir shows clearly decreasing trends in the range of  $0^{\circ}$ – $30^{\circ}$  incident angles. My result fits Aleardi and Mazzotti's (2012) previous general conclusions very well, even though they studied fractured geothermal reservoirs in the intrusive basement of the Larderello-Travale geothermal field, Italy.

Carried out an accurate seismic well tie, very good fit between the calculated synthetic and real seismic traces was reached with a correlation coefficient value of 0.807. The P-wave acoustic impedance log inserted in the closest vertical seismic cross-section showed excellent fit between the well log and seismic data after the seismic well tie.

Traditional post-stack P-impedance inversion on the properly pre-processed 3D seismic and well log data provided an appropriate P-impedance model to indicate the investigated hot water bearing dolomitic fracture zone located in the Triassic basement. The inverted model resulted in anomalously low acoustic impedance values at the fractured interval revealed by a production well. However, the obtained model was not helpful to understand the horizontally variable lithology of the carbonate basement. For this reason, I carried out other modern pre-stack inversion procedures.

Scaled Poisson's Ratio Change AVO attribute model derived from the pre-stack seismic amplitudes indicated decreasing values at the top of the fractured carbonate zone and

increasing values at its base. This feature of the Poisson's ratio is very characteristic for the fluid saturated zones in any porous geological formations. P-wave impedance, as well as P- and S-wave velocity ratio attribute obtained by the pre-stack Simultaneous Model-based inversion were also useful to map the hot water bearing porous zones of the basement. However, separation of the dolomite fracture zones, and the Triassic marl was not very successful by the above-mentioned inverted rock physical attributes. None the less, the P- and S-wave velocity ratio turned out to be as a good indicator for both the fracture zones and their complex lithological surroundings in the pre-Cenozoic basement.

The results of the above-mentioned pre-stack AVO and Simultaneous Model-based inversions provided the opportunity to carry out Lamda-Mu-Rho (LMR) transformation, which yielded to get two more characteristic rock physical models related with the Lamé parameters ( $\Lambda \cdot \rho$  and  $\mu \cdot \rho$ ). Studying those characteristic elastic parameters,  $\Lambda \cdot \rho$  proved to be the best amongst all inverted models in my study area, both from the viewpoint of fracture indication and lithology discrimination in the Triassic basement. My conclusion fits to Goodway's (2001) essential statements which were taken on a wide range of geological formations.

Most of the inverted rock physical models calculated and studied in my PhD dissertation were useful to identify and map the fractured zones containing high temperature hot water in the Triassic basement of my study area located in the Little Hungarian Plain, Hungary. Tracking the surrounding lithological formations, for example the Triassic marl was a more difficult task but it became successful after utilizing a subsequent LMR transformation. All inverted rock physical models obtained by the presented inversion procedures are evaluated from practical viewpoint in Table 5.

**Table 5** Evaluation of the inverted rock physical models obtained in the study area

Procedure / Rock physical model	Detection of the fracture zone	Discrimination of the lithology
Post-stack P-impedance inversion - P-wave impedance ( $Z_P$ ):	- Medium	- Poor
Pre-stack AVO inversion - Scaled Poisson's Ratio Change ( $\Delta\sigma$ ):	- Excellent	- Poor
Pre-stack Simultaneous Model-based inversion - P-wave impedance ( $Z_P$ ): - S-wave impedance ( $Z_S$ ): - Density ( $\rho$ ): - P- and S-wave velocity ratio ( $V_P/V_S$ ):	- Medium - Poor - Poor - Excellent	- Poor - Poor - Poor - Good
Lambda-Mu-Rho transformation - Lambda*Rho ( $\lambda\rho$ ): - Mu*Rho ( $\mu\rho$ ):	- Excellent - Poor	- Excellent - Excellent
Cross-plotting - Velocity ratio ( $V_P/V_S$ ) versus P-wave impedance ( $Z_P$ ): - Mu*Rho ( $\mu\rho$ ) versus Lambda*Rho ( $\lambda\rho$ ):	- Excellent - Excellent	- Excellent - Excellent
Spatial mapping - Scaled Poisson's Ratio Change ( $\Delta\sigma$ ): - P- and S-wave velocity ratio ( $V_P/V_S$ ): - Lambda*Rho ( $\lambda\rho$ ):	- Excellent - Excellent - Excellent	- Poor - Poor - Poor

There are several practical benefits of the inverted rock physical models that I presented in my dissertation. They revealed the complex lithology of the Triassic basement and the hot water bearing reservoir system located in its fracture zones. Based on my new results, I concluded that three production wells drilled in the study area years before my recent investigations hit the western part of the geothermal reservoir. According to the investigated models, the major volume of the reservoir is in the eastern direction from those wells, and it has a vertically cyclic fabric of the porous zones. The methodology that I presented in my PhD dissertation is based on sophisticated seismic and well logging inversion algorithms, adopted from the hydrocarbon exploration, and can help with the well planning in future geothermal investigations.

### **Acknowledgements**

I would like to express my deep gratitude to God for His unwavering presence in my life and for blessing me with the opportunity to live and study in Hungary. I am truly grateful for His guidance and the countless blessings that have enriched my academic journey.

My appreciation also goes to my family, whose unconditional love, support, and encouragement have been the foundation of my progress. Their belief in me and their constant motivation had been instrumental in overcoming challenges and pursuing my academic goals.

I extend my heartfelt thanks to the Scholarship Program for Christian Young People (SCYP). SCYP has not only provided me financial assistance, but it has also opened doors to cultural activities and volunteer work.

I would like to express my warmest acknowledgement to my supervisor, Dr. Ernő Takács for his unwavering support, guidance, and expertise that have been invaluable. I am grateful for his dedication and mentorship, without which the completion of my PhD thesis would have not been possible. His encouragement and belief in my abilities have been a constant source of inspiration.

I would like to extend my gratitude to all my professors, advisors, colleagues, and friends who have supported me throughout this journey. Your contributions enriched my research and personal growth.

I thank the former Mining and Geological Survey of Hungary (MBFSZ) for providing me the opportunity to work on this study, which was an integral part of my PhD education. I also thank the present Geological Directorate, Supervisory Authority for Regulatory Affairs (SZTFH) to allow me to complete my studies in the subject of this exciting geothermal investigation. I am very grateful for the Geophysical Department, University of Miskolc to give me every help to achieve the goals assigned in my PhD research plan. I appreciate Geo-Log Ltd. and PannErgy Plc. for their permission to use geophysical data available in my study area.

21 August 2023, Miskolc

Emad Nageh Masri Abdelnour

**References**

- Aki K. and Richards P.G. (1980): Quantitative seismology – Theory and methods. Volume 1, WH Freeman and Company, 557 p.
- Aleardi M. and Mazzotti A. (2012): A study on the seismic AVO signatures of deep fractured geothermal reservoirs in an intrusive basement. Geophysical Research Abstracts, Vol. 14, EGU General Assembly 2012.
- Allen J.L. and Peddy C.P. (1993): Amplitude Variation with Offset: Gulf Coast Case Studies. Society of Exploration Geophysics, Geophysical Development Series, 4.
- Allo F., Coulon J.P., Formento J.L., Reboul R., Capar L., Darnet M., Issautier B., Marc S., and Stopin A (2021): Characterization of a carbonate geothermal reservoir using rock-physics-guided deep neural networks. The Leading Edge 40, 751–758.
- Békési E., Lenkey L., Limberger J., Porkoláb K., Balázs A., Bonté D., Vrijlandt M., Horváth F., Cloetingh S., and van Wees J.D. (2018): Subsurface temperature model of the Hungarian part of the Pannonian Basin. Global and Planetary Change 171, 48–64.
- Biot M.A. (1956): Theory of propagation of elastic waves in fluid-saturated porous solids II – Higher frequency range. Journal of the Acoustical Society of America 28, 179–191.
- Castagna J.P., Batzle M., and Eastwood R.L. (1985): Relationships between compressional-wave and shear-wave velocities in clastic silicate rocks. Geophysics 50, 571–581.
- Chopra S., and Castagna J.P. (2014): AVO, Investigations in Geophysics 16, Society of Exploration Geophysicist, Tulsa, Oklahoma, 288 p.
- Cserkész-Nagy Á., Bauer M., Takács E., Csabafi R., Gúthy T., Kóborné Bujdosó É., Török I., †Redlerné Tátrai M., Szóts G., Kovács A.Cs, and Hegedűs E (2020): Significance of the reflection seismic methods in minimizing the geological uncertainty of non-hydrocarbon explorations in Hungary (in Hungarian with English abstract and figure captions). Földtani Közlöny 150, 151–168.
- Dolton G.L. (2006): Pannonian Basin Province, Central Europe (Province 4808) – Petroleum Geology, Total Petroleum Systems, and Petroleum Resource Assessment. USGS Bulletin 2204–B, 47 p.

- Fatti J.L., Smith G.C., Vail P.J., Strauss P.J., and Levitt P.R. (1994): Detection of gas in sandstone reservoirs using AVO analysis: A 3-D seismic case history using the geostack technique. *Geophysics* 59, 1362–1376.
- Fodor L., Koroknai B., Balogh K., Dunkl I., and Horváth P. (2003): Nappe position of the Transdanubian Range Unit ('Bakony') based on new structural and geochronological data from NE Slovenia (in Hungarian with English abstract and figure captions). *Földtani Közlöny* 133, 535–546.
- Gardner G.F.H., Gardner L.W., and Gregory A.R. (1974): Formation velocity and density. The diagnostic basics for stratigraphic traps. *Geophysics* 39, 770–780.
- Gassmann F. (1951): Über die Elastizität poroser Medien [On elasticity of porous media]. *Vierteljahrsschrift der Naturforschenden Gesellschaft in Zürich* 96, 1–23.
- Geertsma J. and Smit D.C. (1961): Some aspects of elastic wave propagation in fluid-saturated porous solids. *Geophysics* 26, 169–181.
- Goodway B. (2001): AVO and Lamé constants for rock parameterization and fluid detection. *CSEG Recorder* 26, 39–61.
- Haas J., Budai T., Csontos L., Fodor L., Konrád G., and Koroknai B. (2014): Geology of the pre-Cenozoic basement of Hungary. Explanatory notes for “Pre-Cenozoic geological map of Hungary (1:500,000)”. A publication of the former Geological Institute of Hungary, 71 p.
- Hampson D.P., Russell B.H., and Bankhead B. (2005): Simultaneous inversion of pre-stack seismic data. 75th Annual International Meeting, SEG, Expanded Abstracts, 1633–1638.
- Hampson-Russell Software Services Ltd. (2006): AVO Guide. CGG Veritas, 85 p.
- Hampson-Russell Software Services Ltd. (2007): STRATA Guide. CGG Veritas, 89 p.
- Harvey P.J. (1993): Porosity identification using AVO in Jurassic carbonate, offshore Nova Scotia. *The Leading Edge* 12, 180–184.
- Kovács A.Cs., Pelczéder Á., Hegedűs E., Prohászka A., Fancsik T., Csabafi R., and Gúthy T. (2019): Largest geothermal investment in NW Hungary by PannErgy. 13th GeoTHERM Expo & Congress, 14-15 February 2019, Offenburg, Germany.
- Landmark Graphics Corporation (2001): ProMAX, A Reference Guide for the ProMAX Geophysical Processing Software, Volume 1 and 2.

- Li Y., Downton J., and Goodway B. (2003): Recent applications of AVO to carbonate reservoirs in the Western Canadian Sedimentary Basin. *The Leading Edge* 22, 670–674.
- Lindseth R.O. (1979): Synthetic logs; a process for stratigraphic interpretation. *Geophysics* 44, 2–26.
- Lloyd H.J.E. and Margrave G.F. (2011): Bandlimited impedance inversion: using well logs to fill low frequency information in a non-homogenous model. *CREWES Research Report*, Volume 23, 1–21.
- Lynch S., Crook H., Peel S., Foster P., and Cowan G. (1997): Carbonate reservoir characterization using 3D AVO – A case study from offshore Tunisia. *Extended Abstracts*, 59th Meeting of EAGE, 26-30 May 1997, Geneva, Switzerland.
- Ma X. (2002): Simultaneous inversion of prestack seismic data for rock properties using simulated annealing. *Geophysics* 67, 1877–1885.
- Mallick S. (2001): Prestack waveform inversion using a genetic algorithm – The present and the future. *CSEG Recorder* 26, 78–84.
- Masri E.N. and Takács E. (2022a): AVO study on a known geothermal reservoir located in the fractured carbonate formations of the pre-Cenozoic basement, Northwest Hungary. *Acta Geodaetica et Geophysica* 57, 477–494. <https://doi.org/10.1007/s40328-022-00387-3>
- Masri E.N. and Takács E. (2022b): Characterization of a carbonate geothermal reservoir by the inversion of seismic reflection amplitudes. *Extended Abstracts*, GET 2022, 3rd EAGE Global Energy Transition Conference and Exhibition, 7-9 November 2022, The Hague, The Netherlands, P66. <https://doi.org/10.3997/2214-4609.202221066>
- Masri E.N., and Takács E (2023): Simultaneous Model-based inversion of pre-stack 3D seismic data targeting a deep geothermal reservoir, Northwest Hungary. *Acta Geodaetica et Geophysica* 58, 19–33. <https://doi.org/10.1007/s40328-023-00404-z>
- Mavko G., Mukerji T., and Dvorkin J. (1998): *The rock physics handbook – Tools for seismic analysis in porous media*. Cambridge University Press, 168–170.
- Mazzotti A. and Mirri S. (1991): An experience in seismic amplitude processing. *First Break*, 9, 65–73.
- Mazzotti A. and Ravagnan G. (1995): Impact of processing on the amplitude versus offset response of a marine seismic data set. *Geophysical Prospecting* 43, 263-281.

- Miles D., Gassaway G., Bennett L., and Brown R. (1989): Three-component amplitude versus offset analysis. *Exploration Geophysics* 20, 257–257.
- Ostrander W.J. (1984): Plane-wave reflection coefficients for gas sands at nonnormal angles of incidence. *Geophysics* 49,1637–1648.
- Pratt T.L., Brown L.D., and Mondary J. (1993): AVO and fluids in the deep crust: A COCORP case study. *The Leading Edge* 12, 186–192.
- Richards P.G. and Frasier C.W. (1976): Scattering of elastic waves from depth dependent inhomogeneities. *Geophysics* 41, 441–458.
- Russell B. (2020): Seismic Exploration and Development for Geothermal Energy. Webinar by Brian Russell, CGG GeoSoftware, 3 November 2020.
- Russell B. and Hampson D. (2006): The old and the new in seismic inversion. *CSEG Recorder* 31, 5–11.
- Russell B.H., Hampson D., and Bankhead B. (2006): An inversion primer. *CSEG Recorder*, Special issue, 96–103.
- Shuey R.T. (1985): A simplification of the Zoeppritz equations. *Geophysics* 50, 609–614.
- Simon M. (1998): AVO analysis by offset-limited prestack migrations of crustal seismic data. *Tectonophysics* 286, 143–153.
- Smith G.C. and Gidlow P.M. (1987): Weighted stacking for rock property estimation and detections of gas. *Geophysical Prospecting* 35, 993–1014.
- Sztanó O., Kováč M., Magyar I., Šujan M., Fodor L., Uhrin A., Rybár S., Csillag G., and Tőkés L. (2016): Late Miocene sedimentary record of the Danube/ Kisalföld Basin: interregional correlation of depositional systems, stratigraphy, and structural evolution. *Geologica Carpathica* 67, 525–542.
- Takács E. and Hajnal Z. (2000): Amplitude Versus Offset case study on the Moho. *Geophysical Transactions* 43, 93–111.
- Takács E., Hajnal Z., Pandit B., and Annesley I.R. (2015): Mapping of alteration zones with seismic-amplitude data and well logs in the hard-rock environment of the Keefe Lake area, Athabasca Basin, Canada. *The Leading Edge* 34, 530-538.

- Takács E., Kemény M., Gúthy T., Hegedűs E., and Fancsik T. (2021): Elastic parameter estimation in the vicinity of Moho using AVO inversion – PGT-4 seismic section (in Hungarian with English abstract and figure captions). *Magyar Geofizika* 62, 73–83.
- Taner M.T., Koehler F., and Sheriff R.E. (1979): Complex seismic trace analysis. *Geophysics* 44, 1041–1063.
- Tari G. (1994): Alpine Tectonics of the Pannonian basin. PhD Thesis, Rice University, Texas, USA: 501 p.
- Tari G. and Horváth F. (2010): Eo-Alpine evolution of the Transdanubian Range in the nappe system of the Eastern Alps: revival of a 15 years old tectonic model (in Hungarian with English abstract and figure captions). *Földtani Közlöny* 140, 463–505.
- Young G.B.L. and Braile W. (1976): A computer program for the application of Zoeppritz's amplitude equations and Knott's energy equations. *Bulletin of the Seismological Society of America* 66, 1881–1885.
- Zoeppritz K. (1919): Über Reflexion und Durchgang seismischer Wellen durch Unstetigkeitsflächen (On the reflection and transmission of seismic waves at surfaces of discontinuity). *Nachrichte von der Königlichen Gesellschaft der Wissenschaften zu Göttingen*, 66–84.